the plant journal

The Plant Journal (2025) **124**, e70604

doi: 10.1111/tpj.70604

N[6]-methyladenosine and poly(A) tail-mediated posttranscriptional regulation in bamboo mosaic virus–*Dendrocalamus latiflorus* interactions

Xiangrong Li[1,†], Lin Wu[2,†], Huihui Wang[2,†], Jun Zhang[1], Xiaoxia Jing[1], Zeyu Zhang[2], Yuhua Wang[1], Huiyuan Wang[2], Wenbiao Liu[1], Ruxue Wang[1], Liangzhen Zhao[1], Hangxiao Zhang[1] and Lianfeng Gu[1,*]

[1]*Basic Forestry and Proteomics Research Center, Fujian Provincial Key Laboratory of Haixia Applied Plant Systems Biology, Fujian Agriculture and Forestry University, Fuzhou 350002, China, and*

[2]*College of Forestry, Fujian Agriculture and Forestry University, Fuzhou 350002, China*

Received 2 July 2025; revised 27 October 2025; accepted 8 November 2025.

*For correspondence (e-mail lfgu@fafu.edu.cn)

[†]These authors contributed equally to this work.

SUMMARY

The economically important bamboo species *Dendrocalamus latiflorus* Munro (*D. latiflorus*) exhibits highly susceptible to Bamboo mosaic virus (BaMV), resulting in severe growth and development impairment. However, the proteomic profiles, transcript processing dynamics, and their coordinated posttranscriptional regulation during bamboo–virus interactions remain uncharacterized. Tandem mass tag (TMT)-based quantitative proteomic revealed suppression of photosynthesis-related proteins and upregulation of protein synthesis and degradation, antioxidant within *D. latiflorus* during BaMV infection. Moreover, the APR1 protein serviced as a regulatory hub for connecting sulfur metabolism, antioxidant, and photosynthesis. Integration of nanopore direct RNA sequencing (DRS) data revealed reduced *D. latiflorus* full-length read ratios, consequently attenuating transcriptome and proteome correlation. BaMV-infected bamboos presented preferential usage of distal poly(A) site and lengthened poly(A) tail lengths (PALs) of pathogenesis-related (PR) genes. Epitranscriptome analysis showed increased N^6-methyladenosine (m^{6}A) ratios in *POR* (chlorophyll synthesis) and *NCED1* (abscisic acid synthesis), which coupled with reduced transcriptional levels. In total, 122 potential m^{6}A modification sites were found in BaMV, with AAACA representing the predominant consensus motif. Collectively, these results offer insights into posttranscriptional regulation networks during bamboo–BaMV interactions.

Keywords: BaMV, *Dendrocalamus Latiflorus*, N^6-methyladenosine, Nanopore direct RNA sequencing, Posttranscriptional, Virus–Host Interaction.

INTRODUCTION

As the most prevalent dynamic modification in eukaryotic mRNA, *N*^{6}-methyladenosine (m^{6}A) has been demonstrated to be extensively involved in the host–virus interactions. Viral mRNA can exploit m^{6}A to stabilize the modified sequences, such as wheat yellow mosaic virus (WYMV) which utilized *TaMTB* to promote viral replication, or as a molecular marker "camouflaged" as endogenous RNA to evade immune surveillance (Lu *et al*., 2020; Zhang et al., 2022). Viral invasion can interfere with host RNA methylation modifications, impacting antiviral functions across pathological systems. For instance, rice black streaked dwarf virus (RBSDV) and rice stripe virus (RSV) infection increased overall m^{6}A levels in rice, particularly in genes associated with RNA silencing and phytohormone metabolism (Zhang et al., 2021). Conversely, cucumber green mottle mosaic virus (CGMMV) infection reduced m^{6}A levels in resistant watermelons, with hypomethylated genes enriched in RNA synthesis and stress response pathways (He et al., 2021). In addition to m^{6}A, pseudouridine (Ψ) is another prevalent RNA modifications occurring in both mRNA and noncoding RNAs (Roundtree et al., 2017; Zhao & He, 2015) and also take place in the sequences of RNA viruses (Campos et al., 2021). Therefore, it will be important to investigate the RNA modifications in host–virus interactions, as it may reveal the epigenetic regulatory mechanisms governing viral infection and host responses.

Recent studies have highlighted the crucial role of posttranscriptional regulation in host–virus interactions

(Jia et al., 2017; Yuan et al., 2023). In addition to RNA modifications, processes including alternative splicing and polyadenylation profoundly affect gene expression and host physiological responses (Engel et al., 2018; Gallegos, 2018; Sadek et al., 2019). Thus, high-resolution transcriptomic profiling is essential to uncover the molecular mechanisms driving host responses to viral infection. Oxford Nanopore's direct RNA sequencing (DRS) enables single-base resolution detection of RNA modifications, accurate poly(A) tail length (PAL), and isoform identification, quantification offering insights into alternative splicing and polyadenylation (Gao et al., 2022; Mulroney et al., 2022; Wang et al., 2021; Yu et al., 2023). Alternative polyadenylation (APA) generates transcript isoforms diversity during pre-RNA processing (; Tian and Manley, 2017a), a posttranscriptional implications for nuclear export, gene expression, eukaryotic cell differentiation and proliferation, as well as stress responses (Floor & Doudna, 2016; Shen et al., 2011; Tian and Manley, 2017b; Wu & Bartel, 2017). In rice, bacterial blight (BB) and RSV infection altered APA events in genes related to chlorophyll metabolism, linked to leaf disease development (Ye et al., 2019). Vesicular stomatitis virus (VSV) infection led to truncated 3′ untranslated regions (3′UTRs) and markedly reducing 3′-end processing factor expression (Jia et al., 2017). Moreover, genes with altered APA profiles and mRNA levels were linked to the host immune response, highlighting APA's pivotal role in antiviral defense. The polyadenylated tail is essential for mRNA stability and translation (Passmore & Coller, 2022). Viruses protect their transcripts by adding non-adenosine nucleotides to the poly(A) tail (Kim, Lee, Jung, et al., 2020). Under homeostatic conditions, highly translated and stable RNAs typically possess shorter poly(A) tails (Passmore & Coller, 2022). Heat-responsive transcripts displayed elongation of the poly(A) tail, accompanied by enhanced protein expression (Wu et al., 2020). However, the regulatory mechanisms of PAL during plant stress remain largely uninvestigated.

Bamboo is an economically important species; yet its growth is severely threatened by Bamboo mosaic virus (BaMV). In susceptible hosts like *D. latiflorus*, BaMV infection causes leaf mosaic symptoms with alternating yellow and green stripes, necrosis in young shoots and stems, and even clump death (Lin et al., 1993, Hsu & Lin, 2004, Nelson & Borth, 2011). As a member of *Potexvirus*, BaMV possesses a 6366 nt positive-sense single-stranded RNA genome, with a 5′m7GpppG cap and 150 ~ 300 nt poly(A) tail (Li et al., 2001). The viral RNA contains five open reading frames (ORFs). After invading host cells, negative strand RNA synthesis, genomic RNA (gRNA) replication, and 3′ co-terminal subgenomic RNAs (sgRNAs) are carried out within chloroplasts, including TGBsgRNA and sgRNA2 for transcription of downstream TGB protein and CPsgRNA for transcription of coat protein (CP), respectively (Cheng & Tsai, 1999; Huang et al., 2021). BaMV imposes substantial damage on bamboo production. Understanding BaMV-bamboo interactions is crucial for developing control measures against this viral pathogen.

In this study, we utilized DRS and TMT proteomics to comprehensively analyzed RNA modifications including m^6A and Ψ, ratio of full-length reads, PAL, and proteome changes in *D. latiflorus* during BaMV infection. Our results indicated that BaMV infection disrupted the correlation between transcription and protein levels. We also found increased m^6A modification of *POR* and *NCED1* accompanied by a decline in transcriptional levels. Moreover, viral infection caused the overall APA sites to shift toward the distal sites. Multiple pathogenesis-related (PR) gene families exhibited an overall longer PAL after BaMV infection. In addition, we identified potential m^6A sites in BaMV sequence, with the preferred motif being AAACA. In summary, these findings provide valuable information for elucidating the involvement of posttranscriptional factors in plant–virus interactions.

RESULTS

DRS transcriptome profiling of BaMV-infected *D. latiflorus*

To investigate *D. latiflorus* responses to viral infection, we collected leaf samples from mock-inoculated (CK) and BaMV-inoculated bamboos for DRS libraries construction. Subsequently, we employed Illumina next-generation sequencing to correct DRS long-read. Sequencing across four MinION flow cells generated a total of 1.9 million long reads. Alignment analysis revealed that 92.70% (CK group) and 67.19% (BaMV group) were mapped to the *D. latiflorus* genome, with 19.14% of infected group reads mapping to the BaMV genome, indicating successful BaMV infection (Figure 1a). Despite the 3′-end bias in DRS reads, coverage analysis showed that the reads almost covered the entire BaMV genome and gradually enriched toward the 3′-end (Figure 1b). The precise alignment of ORF5's initiation site of CPsgRNA, along with increased coverage (Figure 1b), strongly suggested CPsgRNA accumulation in *D. latiflorus*.

BaMV infection reduced the proportion of full-length transcripts

Full-length read ratios are intricately associated with host RNA synthesis and degradation. In *D. latiflorus*, full-length reads presented uniform coverage across the annotated CDS region, while truncated reads accumulate toward the 3′-end (Figure 1c). The proportion of full-length reads decreased from 23.78% (CK) to 22.18% in BaMV-infected samples (Figure 1d), indicating a modest reduction in full-length read. Differential full-length ratios analysis identified 48 genes with increased and 360 with decreased full-length read proportions ($P < 0.05$, Fisher's exact test), indicating that BaMV infection predominantly reduced full-length representation (Figure 1e, Table S1). We analyzed the expression and protein levels of these 408 genes and found that 140 genes and 31 proteins were differentially expressed, respectively. Moreover, most of these genes were characterized by a decrease in full-length proportion accompanied by downregulated expression (Figure S1). Previous studies have reported that *NbTRXh2*, a member of the thioredoxin family targeted TGBp2 to restrict BaMV movement (Chen, Chen, et al., 2018). In *D. latiflorus*, full-length proportion of *DlaTRX1*, another thioredoxin gene involved in regulating cellular oxidative homeostasis, decreased from 34.2 to 22.3% (Figure 1f), highlighting the distinct roles of TRX family genes in antiviral defense and basic metabolic processes. GO enrichment revealed genes with reduced full-length proportions were predominantly associated with energy transport, photosynthesis, and redox processes within chloroplasts (Figure S2). Conversely, genes with increased full-length proportions were primarily associated with mRNA splicing, signal transduction, and endonuclease activity (Figure 1g). Notably, a U1 snRNP splicing factor gene exhibited coordinated increase in both full-length transcript proportion (27.88%) and protein abundance (Figure 1h). Alternative splicing (AS) analysis revealed retention of introns (RI) and alternative 3′ splice site selection (A3SS) as the predominant events (Figure S3a), BaMV infection caused the greatest reduction in A3SS events. Additionally, most transcripts exhibited single AS event (Figure S3b), with A3SS and alternative 5′ splice site selection (A5SS) being the most prevalent combination of multiple AS events. Differentially splicing analysis ($|dPSI| > 0.1$, $P < 0.05$) yielded 129 increased events and 220 decreased splicing levels (Figure 1i), suggesting that BaMV infection may modulate the bamboo splicing process.

BaMV infection altered protein accumulation in *D. latiflorus*

Viral infection induces widespread proteomic changes, with leaves representing essential organs for plant–virus interaction research (Souza et al., 2019). Therefore, we used TMT labeling to quantify leaf proteomes in BaMV-infected and mock-inoculated *D. latiflorus*. Using a cutoff of $P < 0.05$ and fold-change greater than 1.5 as differentially expressed proteins (DEPs), we identified 329 upregulated and 297 downregulated proteins (Figure 2a and Table S2). Key upregulated proteins included ascorbate peroxidase (APX), the growth-regulating transcription factor LBD29, and stress-responsive cathepsin L (CTSL) (Figure 2a). Conversely, immune-related NLR-C3 and peroxidase-regulating PEX11B proteins were downregulated, potentially facilitating BaMV evasion. Through interrogation of the PlantTFDB (Tian et al., 2019), we identified one downregulated and six upregulated transcription factors (TFs) among DEPs (Figure 2b). These TFs homologous to other species regulate diverse processes involved in leaf senescence and intracellular transport, flowering inhibition, light signal regulation, and photoprotective responses, respectively (Guo & Gan, 2006; Lin & Wang, 2004; Pascual et al., 2016; Rauf et al., 2013; Schmitz et al., 2005; Shaikhali et al., 2012). Although the protein abundance of these genes was not detected in proteomic data, transcriptome analysis revealed increased *AAO3* and chlorophyll-degradation-related genes after infection (Figure 2c), consistent with previous research, which has shown that AtNAP activates *AAO3* to promote chlorophyll degradation (Yang et al., 2014).

Upregulated DEPs revealed GO enrichment for ubiquitin-dependent metabolism, proteasome function, translation, regulation of abscisic acid synthesis, heat stress response, and apoptosis-related peptidase inhibition (Figure S4). Downregulated DEPs were enriched for photosynthesis, sugar metabolism, and methylation processes (Figure 2d). Plants actively suppress photosynthesis during immunity, promoting ROS accumulation in chloroplasts to enhance defense (Su et al., 2018). BaMV infection reduced light-harvesting complex (LHC) and oxygen-evolving complex (OEC) protein levels, impairing chloroplast energy capture and light energy conversion (Figure 2e, Table S3). Collectively, these findings indicate that BaMV, like other plant viruses, suppresses bamboo photosynthesis.

We reconstructed the protein–protein interaction (PPI) network of bamboo in response to BaMV using *Oryza sativa* as a reference from STRING database (Szklarczyk et al., 2023). The network encompassed key virus–plant interaction processes, including photosynthetic reactions and carbon fixation, protein translation and transport, protein repair, glutamine biosynthesis, and starch metabolism (Figure 2f, Table S4). High connected hubs included APR1, GLN1-1, RCABP89, and Q2R8U5_ORYSJ. Viral infections typically reprogrammed plant metabolism, especially in sulfur, nitrogen, and antioxidant pathways (Höller et al., 2010; Kogovšek et al., 2016). The sulfur metabolism, APR1, a chloroplast-localized protein linked glutamine-family amino acid biosynthesis and photosynthetic carbon fixation. APR1 might equips bamboo to counter the stress imposed by BaMV infections by modulating antioxidant defenses, protein repair mechanisms, and photosynthetic efficiency. RCABP89 and Q2R8U5_ORYSJ similarly act as key nodes, connecting photosynthesis with glutamine synthesis and protein translation, respectively.

Alterations in transcriptional and proteomic consistency upon BaMV infection

To investigate the concordance between protein and mRNA levels during infection, we used RNA-seq to profile *D. latiflorus* transcriptomic changes upon BaMV infection, identifying 2139 upregulated and 2164 downregulated genes (Table S5). The protein-to-transcript ratio (PTR = FC

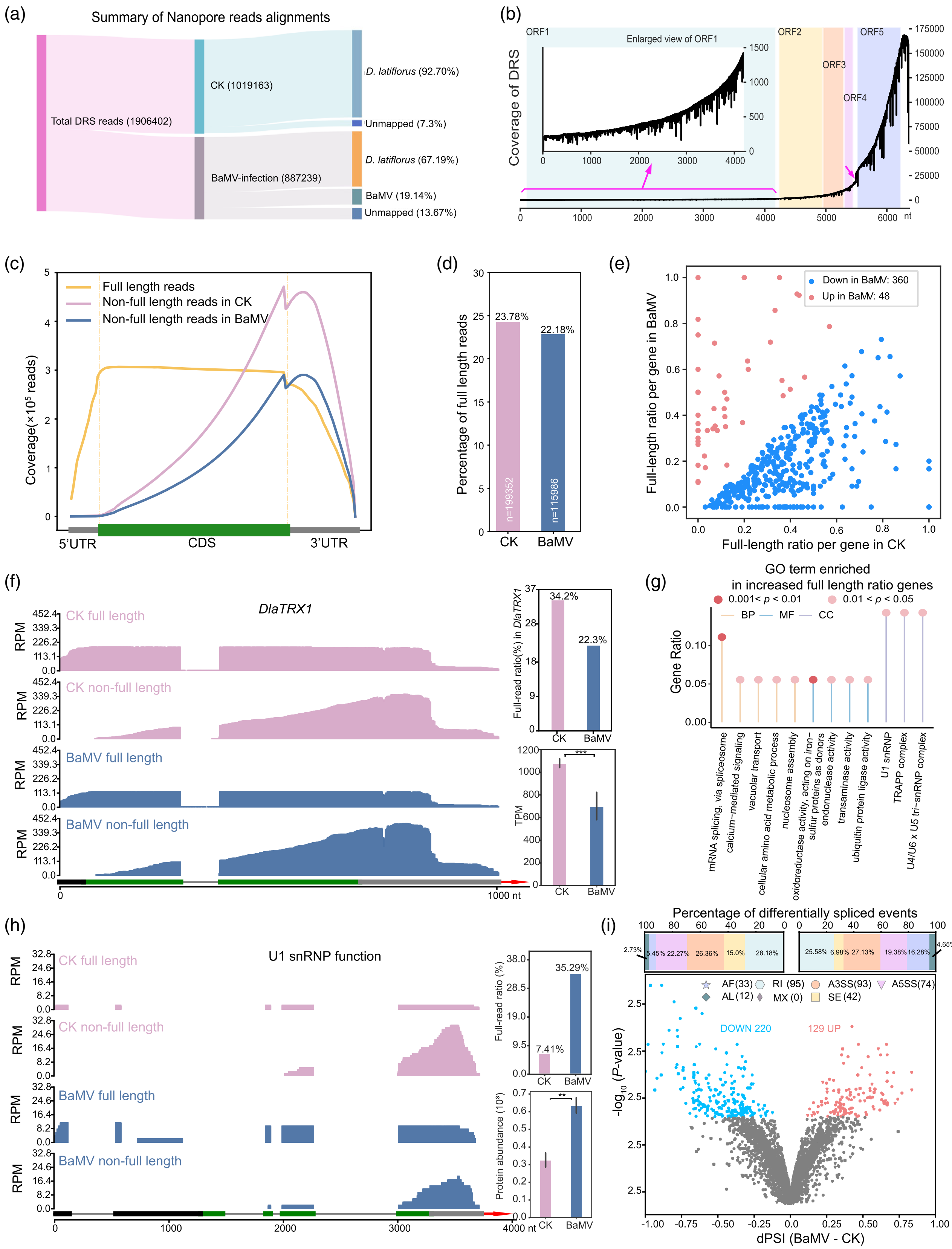
(a)
Summary of Nanopore reads alignments
Total DRS reads (1906402)
CK (1019163)
BaMV-infection (887239)
D. latiflorus (92.70%)
Unmapped (7.3%)
D. latiflorus (67.19%)
BaMV (19.14%)
Unmapped (13.67%)
(b)
ORF1
Enlarged view of ORF1
ORF2
ORF3
ORF4
ORF5
Coverage of DRS
(c)
Full length reads
Non-full length reads in CK
Non-full length reads in BaMV
Coverage(×10⁵ reads)
5'UTR
CDS
3'UTR
(d)
Percentage of full length reads
23.78%
22.18%
n=199352
n=115986
CK
BaMV
(e)
Down in BaMV: 360
Up in BaMV: 48
Full-length ratio per gene in BaMV
Full-length ratio per gene in CK
(f)
DlaTRX1
CK full length
CK non-full length
BaMV full length
BaMV non-full length
RPM
Full-read ratio(%) in DlaTRX1
34.2%
22.3%
TPM
(g)
GO term enriched
in increased full length ratio genes
0.001< p < 0.01
0.01 < p < 0.05
BP
MF
CC
Gene Ratio
mRNA splicing, via spliceosome
calcium-mediated signaling
vacuolar transport
cellular amino acid metabolic process
nucleosome assembly
oxidoreductase activity, acting on iron-sulfur proteins as donors
endonuclease activity
transaminase activity
ubiquitin protein ligase activity
U1 snRNP
TRAPP complex
U4/U6 x U5 tri-snRNP complex
(h)
U1 snRNP function
CK full length
CK non-full length
BaMV full length
BaMV non-full length
Full-read ratio (%)
35.29%
7.41%
Protein abundance (10³)
(i)
Percentage of differentially spliced events
AF(33)
RI (95)
A3SS(93)
A5SS(74)
AL (12)
MX (0)
SE (42)
DOWN 220
129 UP
-log10 (P-value)
dPSI (BaMV - CK)

Figure 1. Nanopore sequencing data and full-length read ratio changes upon BaMV infection.
(a) DRS reads statistics for CK and BaMV-infected samples.
(b) Coverage profile of Nanopore sequencing reads across the BaMV genome.
(c) Coverage distribution of full-length and non-full-length reads along transcripts.
(d) Bar plot showing the overall proportion of full-length reads in CK and BaMV.
(e) Scatterplot displaying differential full-length ratios upon BaMV infection.
(f) Wiggle plot and bar chart demonstrating full-length ratio and expression of *DlaTRX1* after infection.
(g) GO enrichment analysis of genes with significantly increased full-length ratios.
(h) Wiggle plot and bar chart showing increase in full-length ratio and protein abundance for a gene with splicing factor activity.
(i) Scatterplot of differential splicing events (|dPSI| >0.1 and $P < 0.05$), with upper bar plot showing proportions of different splicing event types.

protein/FC mRNA) showed median log10 values of 0.01 for all matched genes ($n = 6944$) and −0.004 for non-differentially expressed genes ($n = 5550$) (Figure S5a,b), while 1394 genes with differential expressed genes exhibited a bimodal FC ratio distribution with distinct peaks at −0.245 and 0.23 (Figure S5c). Overlap analysis between DEPs and DEGs revealed 17.93% (59/329) upregulated and 35.0% (104/297) downregulated proteins showed concurrent changes (Figure 2g). Upregulated DEPs showed greater PTR than downregulated DEPs (Figure 2h).

Drought stress reduced transcription–protein correlations (Gao et al., 2022). Here, we measured Pearson correlations (Cor_p) between mRNA from DRS and proteins during BaMV infection. mRNA (RPM-normalized, $\log_2$) and protein (BaMV rep2-normalized, $\log_2$) abundances showed full-length mRNA bimodal in 0 ~ 3, non-full-length median ~ 3.8, and protein median 10.7 (Figure S6). BaMV infection reduced Cor_p for both non-full-length (Figure 2I) and full-length mRNAs (Figure 2J), suggesting BaMV interference with host posttranscriptional regulation and translation processes. Among genes categorized by expression levels, those with high expression (RPM ≥9) had the lowest Cor_p values for non-full-length transcripts (Figure 2I), but the highest Cor_p values for full-length transcripts (Figure 2J).

Next, we clustered full-length and non-full-length transcripts by KEGG pathway enrichment to analyze BaMV infection-induced changes in their Cor_p. Among full-length transcripts (Figure S7), pathways showed higher Cor_p indicating improved transcription–translation coordination, while 45 pathways had 27 lower Cor_p suggesting decoupled regulation. Non-full-length transcripts had increased Cor_p in 61 and decreased in 67 pathways (Figure S8). Interestingly, the correlations of some pathways were reversed in viral infection, for example, the Cor_p of the core component genes of the spliceosome U1 snRNP A (K11091) changed from negative to positive in non-full-length reads (Figure S8). Viral infection disrupts host carbon metabolism, with class I fructose-bisphosphate aldolases, key enzymes in glycolysis and gluconeogenesis (Wu et al., 2013), serving as critical plant–virus interaction targets. Full-length (Figure S9a) and non-full-length transcripts (Figure S9b) in the class I aldolase pathway (K01623) showed reduced Cor_p with BaMV infection, aligning with global correlation trends.

BaMV infection globally increased m^{6}A modification in *D. latiflorus*

Methyltransferase complex components MTA, HAKAI, and YTHDF family members ECT5/ECT6 showed virus-responsive expression (Postnikova & Nemchinov, 2012), highlighting the universal involvement of m^{6}A in plant–virus interactions. We used DRS data to identify modifications at single-nucleotide resolution and detected 24 446 (CK) versus 26 804 (BaMV) m^{6}A sites on 7449 versus 8406 genes, respectively (Figure 3a). Analysis of distribution showed CDS and 3′UTR regions contained >98% of total modified sites (Figure 3b). Median modification ratio increased from 0.43 (CK) to 0.46 (BaMV) further demonstrated global m^{6}A upregulation (Figure 3c). BaMV upregulated m^{6}A writer gene *Virilizer_B1* and downregulated m^{6}A eraser gene *ALKBH10B(10A)_B1* at the transcriptional level (Figure 3d and Table S6). Proteomic data indicated that the protein abundance of *WTAP_C1* increased 1.6-fold after BaMV infection. The changes of these writer and eraser genes likely contribute to the elevated m^{6}A modification under BaMV infection.

Reader protein YTHDF2 binds to m^{6}A sites to promote mRNA degradation (Wang et al., 2014). In addition, YTHDF3 acts in concert with YTHDF1 to enhance the translation of target mRNAs (Li et al., 2017). BaMV upregulated the expressions of two YTHDF2 and one YTHDF3 genes suggesting these changes may influence mRNA stability and translation efficiency. Moreover, BaMV also induced m^{6}A modifications of the regulatory factors themselves. Four regulatory factors (*HAKAI_A1*, *WTAP_A1*, *YTHDC1_B1*, and *YTHDF2_A1b*) acquired specific modification sites (Figure S10).

The hypersensitive response mediated by resistance (R) genes is a pivotal mechanism of host resistance (Sett et al., 2022). We identified 364 R genes in *D. latiflorus*, all belonging to the CC-NBS-LRR (CNL) type and BaMV increased their overall expression (Figure S11a). Notably, 40 CNL genes showed transcript-level upregulation, with *PB-LRR* (phyB-regulated NBS-LRR gene) exhibiting the most pronounced increase at the protein level (Table S7 and Figure S11a), indicating its potential central role in the plant's antiviral defense. Conversely, the expression of *RPS2* (NL type) declined significantly, possibly due to

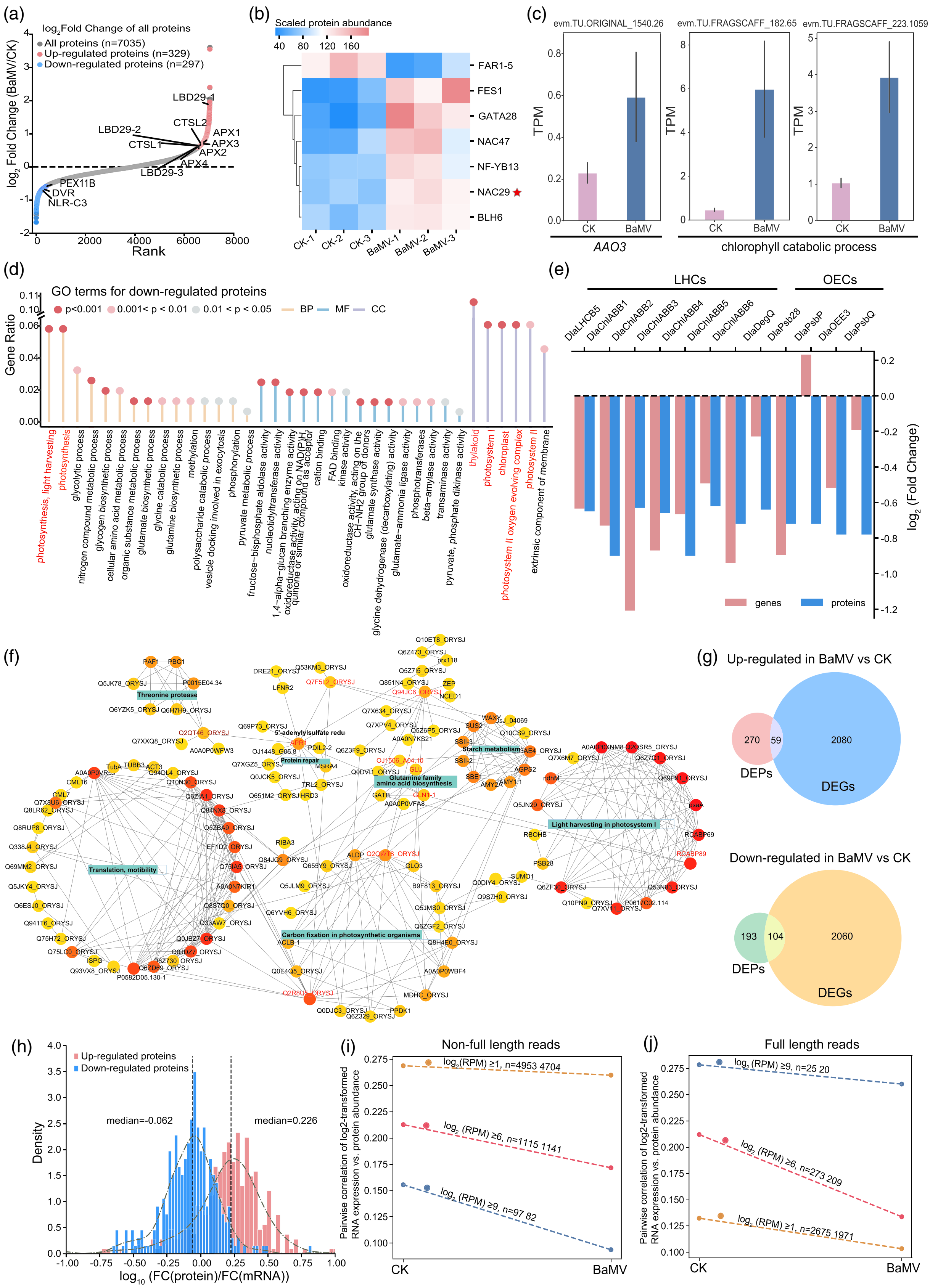
(a)
log2Fold Change of all proteins
All proteins (n=7035)
Up-regulated proteins (n=329)
Down-regulated proteins (n=297)
log2 Fold Change (BaMV/CK)
Rank
(b)
Scaled protein abundance
FAR1-5
FES1
GATA28
NAC47
NF-YB13
NAC29
BLH6
(c)
TPM
AAO3
chlorophyll catabolic process
(d)
GO terms for down-regulated proteins
Gene Ratio
(e)
LHCs
OECs
log2 (Fold Change)
genes
proteins
(f)
(g)
Up-regulated in BaMV vs CK
DEPs
DEGs
Down-regulated in BaMV vs CK
(h)
Up-regulated proteins
Down-regulated proteins
median=-0.062
median=0.226
Density
log10 (FC(protein)/FC(mRNA))
(i)
Non-full length reads
Pairwise correlation of log2-transformed RNA expression vs. protein abundance
(j)
Full length reads

Figure 2. Proteomic changes in *D. latiflorus* under BaMV infection based on mass spectrometry.
(a) Scatterplot of protein fold changes, with red and blue dots representing significantly up- and downregulated proteins (FC >1.5, $P < 0.05$), respectively.
(b) Heatmap showing protein abundance changes of transcription factors.
(c) Bar plot displaying expression changes of *AAO3* and downstream chlorophyll degradation genes.
(d) Lollipop chart of GO enrichment for downregulated proteins.
(e) Bar plot showing FC changes in light-harvesting complex and oxygen-evolving complex proteins.
(f) PPI network of differential proteins, with node size indicating interaction scores and top 10 hub proteins labeled in red.
(g) Venn diagram showing overlap between differentially expressed proteins and genes.
(h) Distribution of PTR ratio ($\log_{10}$ transformed) for up- and downregulated proteins.
(i, j) Correlation between DRS transcript abundance and protein abundance in CK and BaMV infected groups for non-full-length (i) and full-length (j).

BaMV-mediated suppression of host resistance (Table S3). In total, we identified 14 m^{6}A-modified CNL genes (Figure 3e). Further investigation revealed that viral infection elevated the m^{6}A modification levels of CNL genes, paralleling increased expression (Figure 3e). Additionally, the expression levels of hypomethylated genes were relatively lower compared to hypermethylated genes (Figure S11b). Moreover, modification-sites distribution presented a 2.2% increase in the 3′UTR and a 4.5% decrease in the CDS region (Figure S11c).

We classified m^{6}A-modified genes into three categories: constitutively modified genes (CMGs) in both CK and BaMV; and specifically modified genes (SMGs) with expression level RPM >0 in both CK and BaMV, detected only in the control (SMGs-CK) or only in infected samples (SMGs-BaMV). We identified 6252 CMGs, 981 SMGs-CK, and 1891 SMGs-BaMV. Specific modification sites from SMGs showed higher m^{6}A levels (Figure 3f) but lower gene expression (Figure S12a,b) than CMGs. The changes in site modification ratios of CMGs and SMGs after BaMV infection were consistent with the changes in overall modification ratios. SMG m^{6}A sites were more enriched near the 3′ end (Figure S12c). SMGs-BaMV were significantly enriched in autophagy-related processes, suggesting antiviral defense (Figure 3g and Figure S12d).

We identified differentially m^{6}A sites at single-nucleotide resolution in *D. latiflorus* under BaMV infection (Table S8). BaMV induced 528 hyper- and 165 hypomethylated sites, corresponding to 461 and 154 genes, respectively, suggesting that *D. latiflorus* may enhance m^{6}A methylation in response to BaMV invasion (Figure 3h). Motif analysis revealed that hypomethylated sites were enriched in the GGACA motif associated with ubiquitin-dependent protein metabolism, calcium signaling, protein transport, lipid biosynthesis, and photosystem activity (Figure S13). Differential m^{6}A sites showed enrichment in the CDS region and near the stop codon (Figure 3i). GO enrichment analysis of hypermethylated genes revealed terms associated with photosynthesis, superoxide metabolism, the TCA cycle, protein processing, and redox regulation (Figure S14a). Hypomethylated genes were linked to photosynthesis, arabinose metabolism, energy production, and antioxidant activity (Figure S14b).

We integrated m^{6}A, transcriptomic and proteomic datasets to explore their interplay during BaMV infection. The main category showed elevated RNA modifications associated with decreased transcription and protein levels (Figure 3j, Table S9). Notably, several genes or proteins in the fourth quadrant (hyper-down) are involved in m^{6}A-mediated host–virus interactions. BaMV infection can cause chlorosis symptoms in bamboo, which are often attributed to disrupted chlorophyll biosynthesis or excessive accumulation of ROS (Khanna-Chopra, 2012; Lan et al., 2010; Liu et al., 2014; Shimura et al., 2011). Virus-induced ROS accumulation in host plants is commonly counteracted by peroxidases, which play crucial roles in ROS detoxification and enhancing plant resistance (Jiang et al., 2023; Navrot et al., 2006). The glutathione peroxidase gene *GPx* showed hypermethylation and downregulated expression (Figure 3j). Chlorophyll genes MgPME cyclase and protochlorophyllide reductase (*POR*) exhibited hypermethylation accompanied by reduced expression (Figure 3k). These findings indicated that m^{6}A-mediated regulation may influence symptom by modulating the expression of genes involved in chlorophyll biosynthesis and antioxidant defense.

Previous studies have shown that *ABA2* involved in viral accumulation (Alazem et al., 2014). BaMV infection also modulated the abscisic acid (ABA) biosynthesis pathway in *D. latiflorus*. The expression of the upstream ABA biosynthetic genes *DlaZEP* (zeaxanthin epoxidase) and *DlaNCED*s (9-cis-epoxycarotenoid dioxygenases) were downregulated, while *DlaAO3* and its downstream genes were upregulated (Figure 3l). Meanwhile, ABA degradation genes, including the receptor gene *DlaPYL9* and ABA 8′-hydroxylase gene *DlaCYP707A5*, were downregulated, potentially altering the levels of ABA (Figure 3l). Additionally, we observed that the m^{6}A modification of *DlaNCED1* was significantly increased in the 3′UTR region, while the modification of *CYP71A19* in the CDS region was decreased indicating position-specific effects (Figure 3m, Figure S15).

Pseudouridine modification dynamics during viral infection

Pseudouridine (Ψ) is the second most abundant internal modification in mRNA (Li et al., 2015; Ramakrishnan

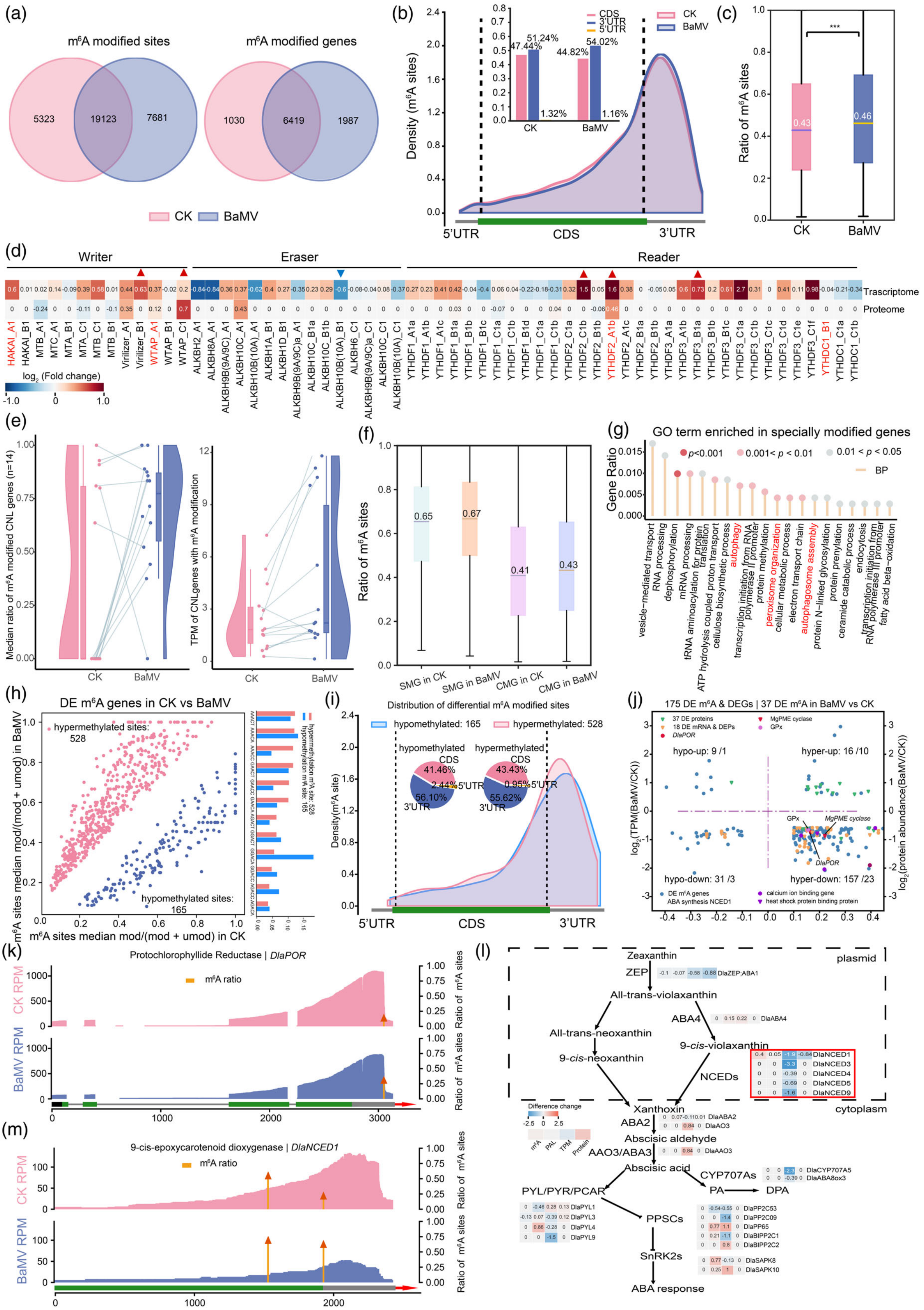
(a)
m6A modified sites
5323
19123
7681
m6A modified genes
1030
6419
1987
CK
BaMV
(b)
Density (m6A sites)
CDS
3'UTR
5'UTR
47.44%
51.24%
1.32%
44.82%
54.02%
1.16%
CK
BaMV
(c)
Ratio of m6A sites
0.43
0.46
***
(d)
Writer
Eraser
Reader
Trascriptome
Proteome
log2 (Fold change)
(e)
Median ratio of m6A modified CNL genes (n=14)
TPM of CNLgenes with m6A modification
(f)
Ratio of m6A sites
0.65
0.67
0.41
0.43
SMG in CK
SMG in BaMV
CMG in CK
CMG in BaMV
(g)
GO term enriched in specially modified genes
Gene Ratio
p<0.001
0.001< p < 0.01
0.01 < p < 0.05
BP
(h)
DE m6A genes in CK vs BaMV
hypermethylated sites: 528
hypomethylated sites: 165
m6A sites median mod/(mod + umod) in BaMV
m6A sites median mod/(mod + umod) in CK
(i)
Distribution of differential m6A modified sites
hypomethylated: 165
hypermethylated: 528
Density(m6A site)
(j)
175 DE m6A & DEGs | 37 DE m6A in BaMV vs CK
hypo-up: 9 /1
hyper-up: 16 /10
hypo-down: 31 /3
hyper-down: 157 /23
log2(TPM(BaMV/CK))
log2(protein abundance(BaMV/CK))
(k)
Protochlorophyllide Reductase | DlaPOR
m6A ratio
CK RPM
BaMV RPM
Ratio of m6A sites
(l)
plasmid
cytoplasm
Zeaxanthin
ZEP
All-trans-violaxanthin
All-trans-neoxanthin
ABA4
9-cis-neoxanthin
9-cis-violaxanthin
NCEDs
Xanthoxin
ABA2
Abscisic aldehyde
AAO3/ABA3
Abscisic acid
CYP707As
PA
DPA
PYL/PYR/PCAR
PPSCs
SnRK2s
ABA response
(m)
9-cis-epoxycarotenoid dioxygenase | DlaNCED1
m6A ratio
CK RPM
BaMV RPM

Figure 3. BaMV-induced m^{6}A modifications alterations in *D. latiflorus*.
(a) Venn diagram of m^{6}A-modified sites and genes in CK versus BaMV groups.
(b) Density plot and bar chart showing distribution and proportions of m^{6}A sites on annotated genes.
(c) Box plot of overall modification ratio (*t*-test, ***$P < 0.001$).
(d) Heatmap of m^{6}A regulator changes at transcript and protein levels and genes.
(e) Raincloud plot showing modification ratios and expression of CNL-type genes with m^{6}A.
(f) Box plot comparing modification ratios between group-specific and shared modified sites.
(g) Top 20 enriched biological processes for specially modified genes upon BaMV infection.
(h) Scatterplot of differential modified sites and bar plot presented motif frequency for hypo- and hypermethylated sites.
(i) Density plot of differential sites along transcripts.
(j) Association analysis between differential modifications and expression/protein changes.
(k) Wiggle plots of m^{6}A site and expression of *DlaPOR*.
(l) ABA pathway with heatmaps of m^{6}A, PAL, TPM, and protein changes.
(m) Wiggle plot of m^{6}A site and expression of *DlaNCED1*.

et al., 2022), playing important roles in translation regulation and mRNA stability (Kierzek et al., 2014; Schwartz et al., 2014). We used NanoSPA (Li et al., 2025) to detect Ψ sites from DRS data and identified 7071 and 4319 Ψ sites in the control (CK) and BaMV-infected groups, respectively. Among these, 2520 Ψ sites were uniquely detected in the BaMV group (Figure S16a and Table S10). The distribution of Ψ sites across transcript regions was uneven, with predominant enrichment in 3′UTR (Figure S16b).

Multiple coexisting modifications frequently occur on the same RNA molecule, exemplifying the complexity of epitranscriptomic regulation. By simultaneously profiling m^{6}A and Ψ modifications, we explored their potential interplay under BaMV infection. Over half of the modified transcripts contained at least one or two m^{6}A or Ψ sites, and transcripts bearing more than five m^{6}A sites were more common than those with multiple Ψ sites (Figure S16c). Genes with co-occurring m^{6}A and Ψ exhibited higher expression levels than those with only one type of modification. Furthermore, these dual-modified genes displayed higher expression in BaMV-infected group compared to the CK group (Figure S16d). Notably, co-occurring m^{6}A and Ψ sites showed nonrandom spatial distance, suggesting potential coordination (Figure S16e). GO enrichment analysis of BaMV-specific Ψ-modified genes revealed significant enrichment in photosynthesis, protein degradation, and translation initiation processes (Figure S17).

Global alteration in poly(A) site usage under BaMV infection

Alternative polyadenylation (APA) is a pivotal posttranscriptional regulation that generates diverse mRNA isoforms with variable 3′UTR lengths (Mayr, 2016; Tian and Manley, 2017b). DRS data revealed 1302 and 673 APA-associated genes in CK and BaMV-infected groups, respectively. The majority of these genes harbored two distinct APA sites (Figure 4a). The length distribution of alternative 3′UTR (aUTRs) in the CK group presented peak at 98 nt, slightly longer than that in the BaMV group (Figure 4b). Among genes with a single polyadenylation site (PAS), the median 3′UTR length in the CK group was longer than that in the BaMV group (Figure 4c). For genes harboring multiple PASs, we selected the two most abundant polyadenylation sites as the proximal (pPAS) and distal (dPAS) PAS. In BaMV-infected samples, we observed more dPAS usage (Figure 4d and Table S11). The log2-transformed ratio between dPAS and pPAS isoform abundance (RED) was 0.12, indicating a global shift toward proximal to distal usage. For example, the *COI1b* gene, encoding a jasmonate receptor critical for disease resistance (Qiu et al., 2022), exhibited an increased distal usage ratio upon BaMV infection (Figure 4e). We identified five categories of core and auxiliary APA-related factors (Table S6 and Figure S18). Notably, *PABPN1*, a known regulator of distal PAS selection (Jenal et al., 2012), was upregulated upon BaMV infection (Figure 4f), possibly contributing to PAS usage and influencing APA regulation under BaMV infection.

GO analysis of APA shifted genes revealed that genes favoring dPAS were enriched in ion transport, mitochondrial energy metabolism and translational elongation, as well as photosynthesis, protein quality control and degradation, and lysine biosynthesis (Figure S19a). In contrast, genes preferring pPAS were involved in photosynthesis, carbohydrate derivative metabolic process, ubiquitin-dependent protein degradation and signal transduction (Figure S19b).

Genes with significant 3′UTR changes upon BaMV infection also exhibited altered protein-to-RNA ratios (PTR ratios, Figure 4g). This result aligns with previous studies which have shown that mRNA 3′UTR length influences protein output (Mayr & Bartel, 2009; Sandberg et al., 2008). Integrative analysis of APA dynamic and proteomics profiles revealed that 68% (17/25) of proteins showed a negative correlation between 3′UTR length and abundance (Figure 4h and Table S12). Notable examples included a redox homeostasis gene, in which a shift toward distal PAS usage coincided with decreased protein and transcript levels (Figure 4i). Conversely, a transcription corepressor gene exhibited a preference for proximal PAS usage

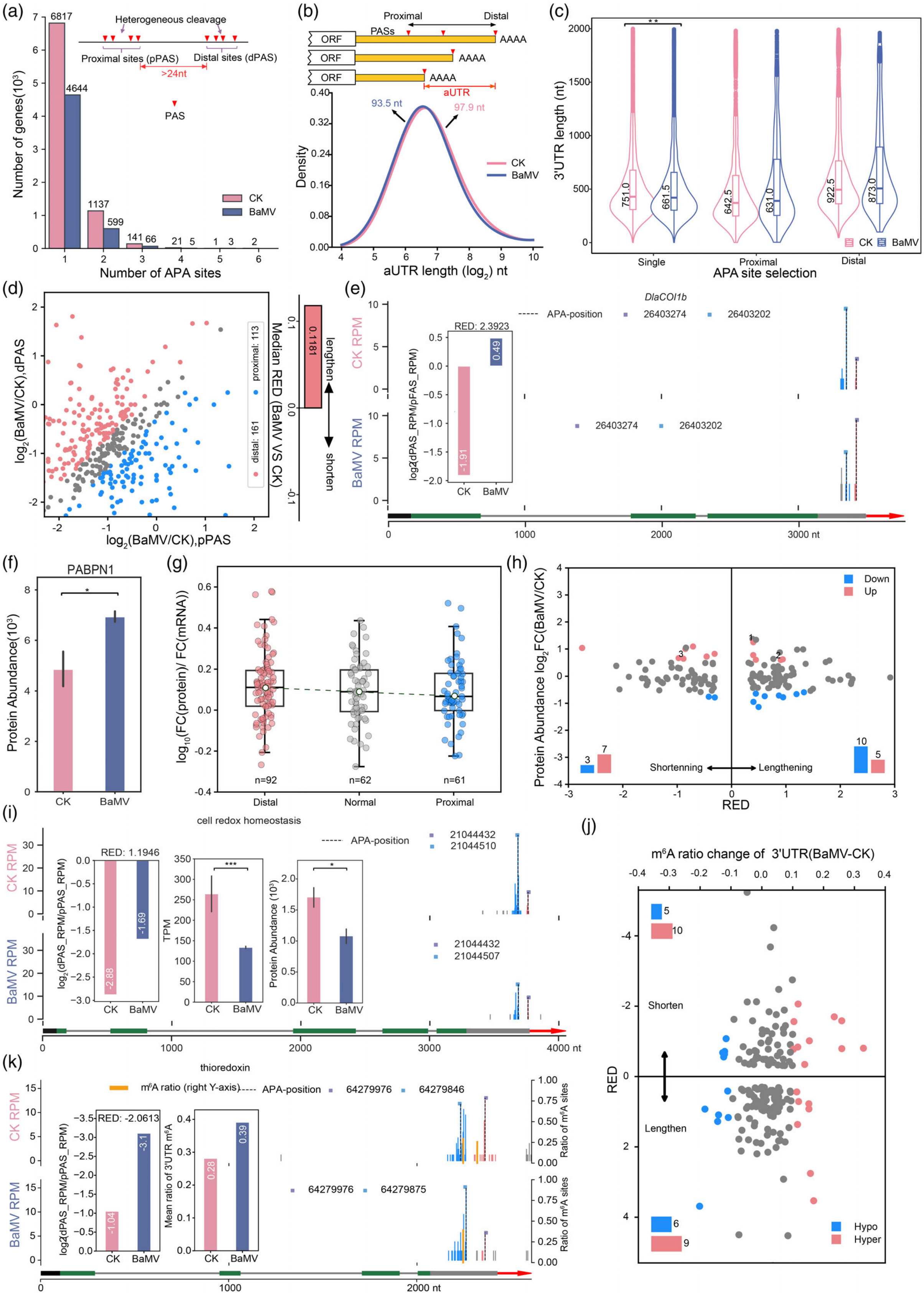

(a)
Heterogeneous cleavage
Proximal sites (pPAS)
Distal sites (dPAS)
>24nt
PAS
Number of genes(10³)
Number of APA sites
CK
BaMV
(b)
Proximal
Distal
PASs
ORF
AAAA
aUTR
93.5 nt
97.9 nt
Density
aUTR length (log₂) nt
(c)
3'UTR length (nt)
Single
Proximal
Distal
APA site selection
(d)
log₂(BaMV/CK),dPAS
log₂(BaMV/CK),pPAS
proximal: 113
distal: 161
Median RED (BaMV VS CK)
lengthen
shorten
(e)
DlaCOl1b
APA-position
26403274
26403202
CK RPM
BaMV RPM
RED: 2.3923
log2(dPAS_RPM/pPAS_RPM)
(f)
PABPN1
Protein Abundance(10³)
(g)
log₁₀(FC(protein)/ FC(mRNA))
n=92
n=62
n=61
Distal
Normal
Proximal
(h)
Protein Abundance log₂FC(BaMV/CK)
Down
Up
Shortenning
Lengthening
RED
(i)
cell redox homeostasis
APA-position
21044432
21044510
21044507
RED: 1.1946
TPM
Protein Abundance (10³)
(j)
m⁶A ratio change of 3'UTR(BaMV-CK)
Shorten
Lengthen
Hypo
Hyper
(k)
thioredoxin
m⁶A ratio (right Y-axis)
64279976
64279846
64279875
RED: -2.0613
Mean ratio of 3'UTR m⁶A
Ratio of m⁶A sites

Figure 4. Global changes in poly(A) site usage upon BaMV infection.
(a) Bar plot of number of genes with different poly(A) clusters (PACs).
(b) Density plot of alternative UTR (aUTR) length distribution.
(c) Violin plot of 3′-UTR length change for genes without APA (Single) and genes with APA (only the proximal most and the distal most 3′-UTR isoforms are plotted, *t*-test, $**0.01 < P < 0.05$). The *y*-axis represents the distance between the poly(A) site and the 3′ end of the last coding sequence (CDS).
(d) Scatterplot of poly(A) changes between proximal (pPAS) and distal (dPAS) sites.
(e) Wiggle plot showing abundance changes of pPAS and dPAS, with bar plot presenting dPAS/pPAS ratio.
(f) Bar plot of PABPN1 protein abundance changes (*t*-test, $*P < 0.05$).
(g) Box plot with jittered scatter plot of PTR ratios associated with PAS usage. The middle line represented the changes in the PTR median.
(h) Scatterplot of associations between differential APA and protein abundance.
(i) Wiggle plot of a gene showing distal PAS usage with decreased expression and protein.
(j) Scatterplot of differential APA-m^{6}A associations in 3′UTRs.
(k) Example gene with proximal PAS usage and increased 3′UTR m^{6}A.

alongside an increased protein level, despite a decrease in its mRNA level (Figure S20), implicating APA as a likely posttranscriptional mechanism enhancing its protein output.

The enrichment of m^{6}A modifications at the 3′ end suggests a possible role in APA-mediated gene regulation. We also observed that some differentially polyadenylated genes exhibited altered m^{6}A modification ratio within their 3′UTRs, particularly those related to protein degradation and redox balance (Figure 4j and Table S12). For instance, thioredoxin encoding gene displayed 3′UTR shortening and increased m^{6}A modification in the 3′UTR region upon BaMV infection (Figure 4k).

Alterations in poly(A) tail length upon viral infection

The 3′ poly(A) tail, an essential nuclear modification during mRNA synthesis, is critical for nuclear export (Colgan & Manley, 1997). Using Nanopore DRS, we assessed PAL changes following BaMV infection. The median PAL increased from 69.97 nt in CK to 74.49 nt in BaMV-infected samples (Figure 5a), indicating a global tail lengthening. In effector-triggered immunity (ETI), one of the downstream responses following effector recognition and signal transduction is the induction of pathogenesis-related (PR) proteins (Cui et al., 2015), originally identified in tobacco infected with tobacco mosaic virus (van Loon & Kammen, 1970). Among 419 identified pathogenesis-related (PR) proteins (Table S6 and Figure S21), specially cysteine-rich secretory protein PR-1, encoding chitinase PR-8, stress-resistance-related PR-5, peroxidase PR-9, and germinoid protein PR 15/16, exhibited PAL extension and increased transcript abundance (Figures 5B and Figure S22a). A subset of these PR transcripts also exhibited changes in m^{6}A modifications and protein level (Figure S22a,c). For example, PR-17-1 and PR-17-2, abscisic acid-inducible secreted proteins, involved in plant–pathogen defense (Kuwabara et al., 1999), which showed notable protein-level induction upon infection (Table S3). In contrast, the immune-related protein PR-1-16 and the peroxidase PR-9-190 exhibited decreased abundance (Table S3).

In total, we identified 123 genes with significantly shortened PAL and 312 genes with significantly lengthened PAL following BaMV infection, suggesting a tendency toward PAL extension in response to BaMV invasion (Figure 5c). For example, a *PR-9-33* gene and *bZIP48* involved in jasmonic acid biosynthesis showed PAL increases of 87.29 nt and 37.63 nt, respectively (Figure 5d). Significant PAL extension was also observed in m^{6}A writer genes (*MTB_B1*, *HAKAI_A1*) and *JAZ7* gene (Figure S23a). Conversely, genes such as poly(A)-binding protein (PabN/-PabI), an antioxidant defense response gene (*BIP130*), and *ALKBH10C_C1* exhibited significant PAL shortening (Figure S23b). GO enrichment showed that genes with PAL extension were associated with transcription initiation, protein synthesis and processing, ABA biosynthesis regulation, and heat response (Figure S24a), while those with PAL shortening were linked to mRNA splicing, drought response, chromatin remodeling, cell division, and proteasome assembly (Figure S24b).

PAL is known to affect mRNA stability and translation efficiency, with shorter tails generally associated with higher transcript abundance (Lima et al., 2017; Subtelny et al., 2014). Correlation analysis revealed 66 DEGs and 19 DEPs that were associated with PAL alterations (Figure 5e and Table S13), with approximately two thirds showing a negative correlation between PAL length and transcript abundance. Of particular interest, the gene encoding the heat shock 70 protein in the second quadrant and the *NPR1* gene regulating ABA synthesis in the fourth quadrant, indicated a potential PAL-associated regulation of their transcript levels upon BaMV infection.

Through Pearson correlation coefficient analysis, we evaluated the relationships among PAL length, transcript abundance, and protein abundance (Figure 5f). A subtle negative correlation was observed between PAL length and transcript abundance (RPM). In contrast, PAL exhibited minimal correlation with protein abundance, indicating limited influence. We also observed a weak correlation between full-length ratio and expression (Figure S25). To further explore the link between PAL and full-length ratio, an indicator of transcript half-lives, we found that full-length reads

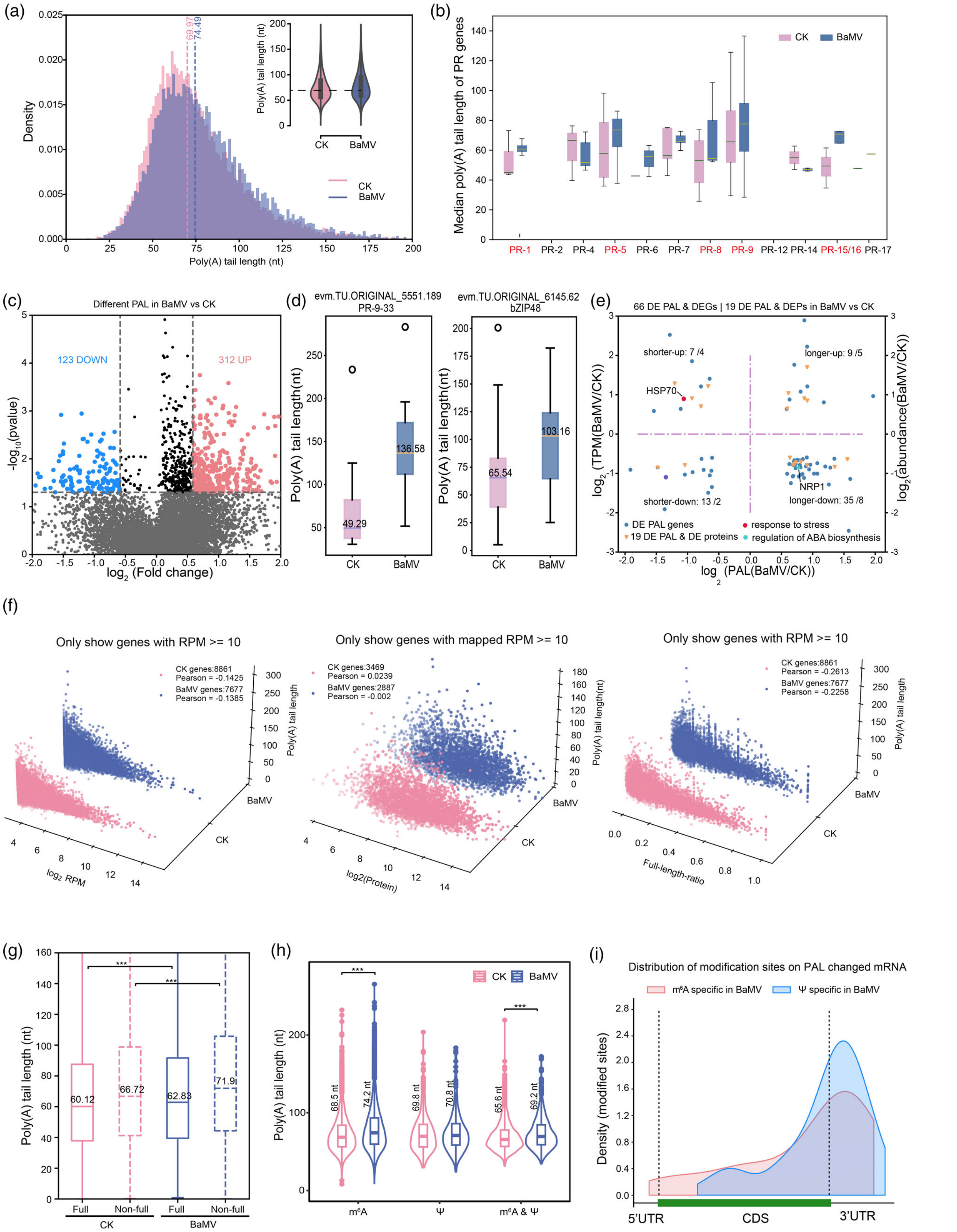

(a)
Density
Poly(A) tail length (nt)
69.97
74.49
CK
BaMV
(b)
Median poly(A) tail length of PR genes
CK
BaMV
PR-1 PR-2 PR-4 PR-5 PR-6 PR-7 PR-8 PR-9 PR-12 PR-14 PR-15/16 PR-17
(c)
Different PAL in BaMV vs CK
123 DOWN
312 UP
-log10(pvalue)
log2 (Fold change)
(d)
evm.TU.ORIGINAL_5551.189
PR-9-33
evm.TU.ORIGINAL_6145.62
bZIP48
Poly(A) tail length(nt)
49.29
136.58
65.54
103.16
CK
BaMV
(e)
66 DE PAL & DEGs | 19 DE PAL & DEPs in BaMV vs CK
shorter-up: 7 /4
longer-up: 9 /5
HSP70
NRP1
shorter-down: 13 /2
longer-down: 35 /8
DE PAL genes
19 DE PAL & DE proteins
response to stress
regulation of ABA biosynthesis
log2 (TPM(BaMV/CK))
log2(abundance(BaMV/CK))
log2 (PAL(BaMV/CK))
(f)
Only show genes with RPM >= 10
CK genes:8861
Pearson = -0.1425
BaMV genes:7677
Pearson = -0.1385
Poly(A) tail length
log2 RPM
Only show genes with mapped RPM >= 10
CK genes:3469
Pearson = 0.0239
BaMV genes:2887
Pearson = -0.002
Poly(A) tail length(nt)
log2(Protein)
Only show genes with RPM >= 10
CK genes:8861
Pearson = -0.2613
BaMV genes:7677
Pearson = -0.2258
Full-length-ratio
(g)
Poly(A) tail length (nt)
60.12
66.72
62.83
71.9
Full
Non-full
CK
BaMV
(h)
Poly(A) tail length (nt)
CK
BaMV
68.5 nt
74.2 nt
69.8 nt
70.8 nt
65.6 nt
69.2 nt
m6A
Ψ
m6A & Ψ
(i)
Distribution of modification sites on PAL changed mRNA
m6A specific in BaMV
Ψ specific in BaMV
Density (modified sites)
5'UTR
CDS
3'UTR

Figure 5. Host PAL changes and potential associations post infection.
(a) Density and violin plots of PAL length distributions.
(b) Box plot of median PAL changes in various PR gene types.
(c) Volcano plot of differential PAL changes.
(d) Box plots of PAL changes in *PR-9-33* and *bZIP48*.
(f) Scatterplots of PAL correlations with expression, protein, and full-length ratios.
(g) Box plot of PAL changes for full-length and non-full-length reads (*t*-test, $^{***}P < 0.001$).
(h) Violin plot of PAL changes for genes with different modification type (*t*-test, $^{***}P < 0.001$).
(i) Distribution of BaMV-specific modified sites on PAL-changed (1.5-fold) transcripts.

had shorter PALs than non-full-length reads (Figure 5g), in line with previous findings that transcripts with longer half-lives tend to have shorter PALs (Chang et al., 2014). Additionally, both full-length and non-full-length reads in BaMV-infected samples had slightly longer PALs than those in CK samples (Figure 5g), consistent with the overall PAL extension observed upon infection.

We also investigated the relationship between PAL and RNA modifications. Transcripts containing m^{6}A modifications exhibited increased median PALs after BaMV infection, whereas those Ψ modified transcripts showed similar median PALs (Figure 5h). Both m^{6}A and Ψ specific sites in BaMV from PAL-altered transcripts were enriched in the 3′UTR region (Figure 5i).

Multilayered posttranscriptional regulation following viral infection

Given that various factors (m^{6}A, Ψ, PAL, and APA) modulate mRNA metabolism to influence transcript and translation, we performed a global correlation analysis to decipher the interplay among each factor. We first quantified the overlap ratio between each factor, finding that DEGs showed the highest overlap with DEPs. Among these regulatory factors, m^{6}A exhibited the strongest association with both DEGs and DEPs (Figure S26). We further classified genes into different types. For instance, 17% of annotated genes were found to harbor m^{6}A modifications, which were subsequently classified into five types according to their modification profiles. BaMV-specific modified genes constituted the largest proportion (Figure 6a and Table S14). In the subsequent analysis, each pie chart represented the ratio of the number of overlapping genes to the total number of genes in the corresponding factors. Association analyses of these gene types revealed that DEGs associated with m^{6}A-specific modifications were the most abundant (Figure 6b). Next, we analyzed cross-factor correlations among altered transcripts (Figure 6c). Among DEGs and DEPs, 1.14% of DEGs and 1.6% of DEP-associated transcripts were co-regulated by two factors. Notably, 26% of transcripts with APA changes exhibited associations with other regulatory factors, suggesting that APA-altered transcripts are particularly susceptible to multilayered regulation during BaMV infection. Collectively, these results demonstrate that posttranscriptional regulatory factors dynamically reshape transcript/protein abundances, with multifactor coordination in virus–host interactions.

We further classified differentially expressed transcripts and proteins based on their associations with the four regulatory factors (m^{6}A, Ψ, PAL, and APA). The pie chart on the right displayed the proportion of overlapping genes/proteins with two categories: genes regulated by a single factor (e.g., differential m^{6}A, Ψ, APA, or PAL only), and those regulated by multiple factors (e.g., genes with both differential m^{6}A and differential PAL) (Figure 6d). The results revealed that 13% of DEGs and 22% of DEPs were associated with regulatory factors, with Ψ accounting for the most associations (Figure 6d). These 13% of DEGs were predominantly enriched in biological processes involving translation element, zinc finger transcription factors regulating plant flowering, inositol metabolism, and stress responses (Figure S27). Among multifactor regulated transcripts, the jasmonate signaling repressor (JAZ), a key component in plant defense and stress resilience, exhibited downregulated expression associated with loss of m^{6}A modification sites in the CDS and elongation of PAL (Figure 6e and Table S15). For 22%, DEPs were primarily associated with translation elongation factors, fructose-bisphosphate aldolase activity, and thioredoxins that maintain redox homeostasis (Figure S27 and Table S15).

M^{6}A profile and PAL of BaMV genomic and subgenomic RNA

BaMV produces three 3′-coterminal sgRNAs, namely TGBsgRNA, sgRNA2, and CPsgRNA, initiating 11 ~ 16 nt upstream of ORF2, ORF3, and ORF5 start codons respectively (Lee et al., 1998). Therefore, the lengths of the generated sgRNAs follow the order of TGBsgRNA > sgRNA2 > CPsgRNA. To avoid frequent 5′-end degradation interference complicating sgRNA discrimination, we analyzed only full-length reads mapping to subgenomic regions. Reads were assigned to specific sgRNAs based on alignment to annotated transcription start sites and the 3′UTR of the BaMV genome. This approach identified 37 reads for TGBsgRNA, 191 for sgRNA2, and 8927 for CPsgRNA. Additionally, 1325 reads spanning the 5′UTR/ORF1 to the 3′UTR were classified as gRNA. Remaining reads were labeled “undefined” (Table S16).

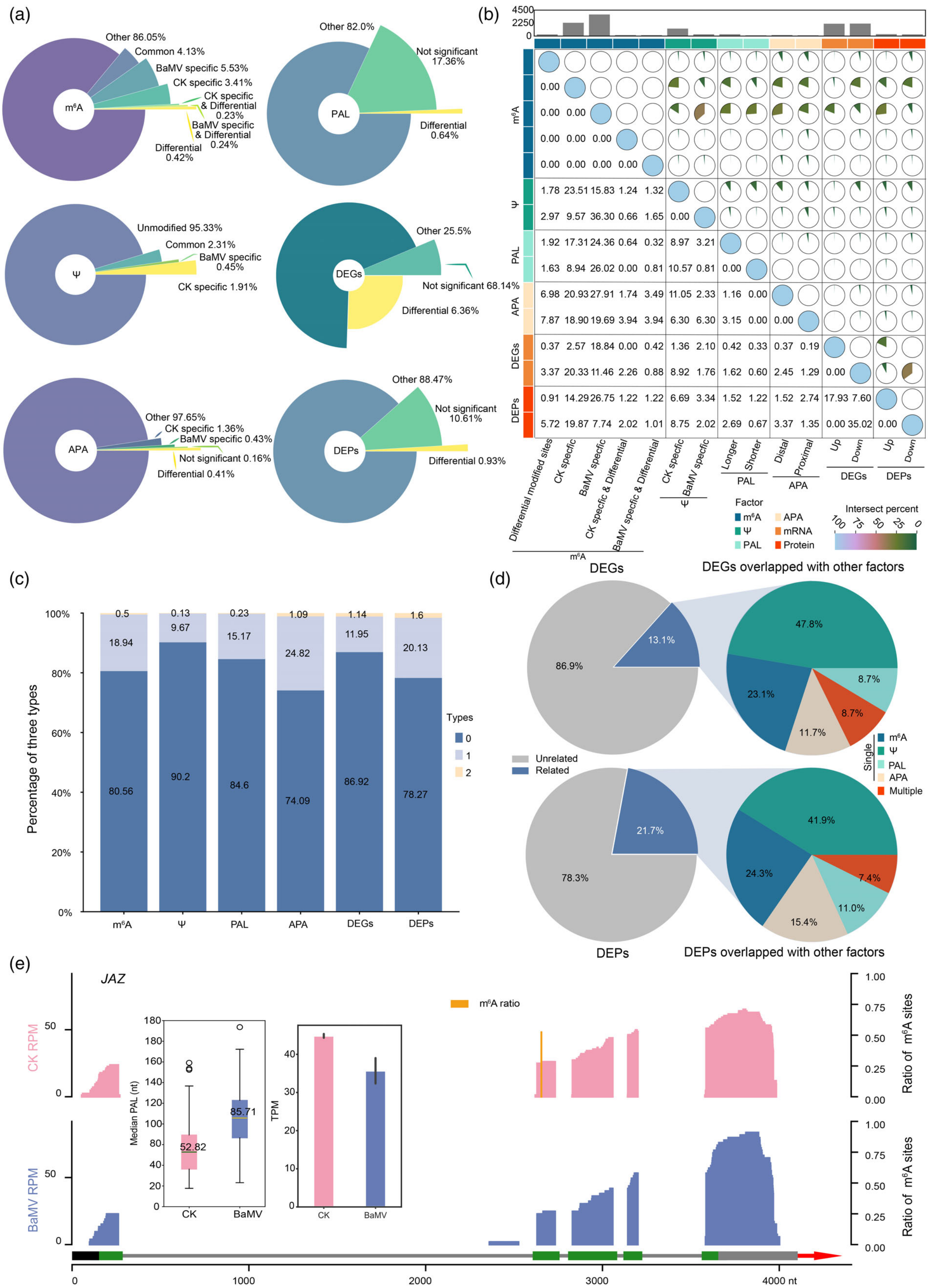
(a)
m6A
Other 86.05%
Common 4.13%
BaMV specific 5.53%
CK specific 3.41%
CK specific & Differential 0.23%
BaMV specific & Differential 0.24%
Differential 0.42%
PAL
Other 82.0%
Not significant 17.36%
Differential 0.64%
Ψ
Unmodified 95.33%
Common 2.31%
BaMV specific 0.45%
CK specific 1.91%
DEGs
Other 25.5%
Not significant 68.14%
Differential 6.36%
APA
Other 97.65%
CK specific 1.36%
BaMV specific 0.43%
Not significant 0.16%
Differential 0.41%
DEPs
Other 88.47%
Not significant 10.61%
Differential 0.93%
(b)
Differential modified sites
CK specific
BaMV specific
CK specific & Differential
BaMV specific & Differential
Longer
Shorter
Distal
Proximal
Up
Down
Factor
Intersect percent
mRNA
Protein
(c)
Percentage of three types
Types
(d)
DEGs
DEGs overlapped with other factors
Unrelated
Related
Single
Multiple
DEPs
DEPs overlapped with other factors
(e)
JAZ
CK RPM
BaMV RPM
m6A ratio
Median PAL (nt)
TPM
CK
BaMV
Ratio of m6A sites
4000 nt

Figure 6. Multilayer factors coordination during BaMV infection.
(a) Pie chart of proportions affected by six regulatory layers in each change: "Specific" represents genes containing specific modification sites or multiple PAS sites in that group, while "Differential" means genes with differentially modified sites. "Specific & Differential" indicates that the gene contains sites that have both of the above characteristics. "Common" represents genes with m^6A or pseudouridine modifications in both BaMV and CK groups.
(b) Pie charts showing pairwise intersections of genes across six regulatory layers: m^6A modifications (differential and condition-specific sites), Pseudouridine (Ψ; CK- or BaMV-specific sites), poly(A) tail length (PAL; longer/shorter tails), alternative polyadenylation (APA; distal vs. proximal site usage), differentially expressed genes (DEGs; up-/downregulated), and differentially expressed proteins (DEPs; up-/downregulated).
(c) The bar plot displays the proportion of regulatory factor interactions, categorized as: Type 0 (isolated changes involving the single factor only), Type 1 (co-occurrence with one additional factor), and Type 2 (Overlaps involving two additional factors).
(d) Pie charts showing the proportion of DEGs and DEPs that overlap with other regulatory factors.
(e) Wiggle plot of JAZ gene showing m^6A loss, PAL lengthening, and decreased expression.

We identified m^6A modification sites in BaMV gRNA and sgRNAs. The median m^6A modification ratio of BaMV ranged from 0.13 to 0.18 and tended to decrease with shorter RNA lengths (Figure 7a). Among assigned reads, we identified 122 potential m^6A modification sites, distributed across gRNA (122 sites), TGBsgRNA (37 sites), sgRNA2 (24 sites), and CPsgRNA (20 sites) (Figure 7b). Among all detected modification sites, AAACA was the most frequent motif. Notably, the motif AAACC accounted for 17.95% of CPsgRNA motifs versus 7.12, 10.14, and 12.71% in gRNA, TGBsgRNA, and sgRNA2, respectively (Figure 7c).

Plant nucleotidyltransferases and polynucleotide phosphorylases participate in organellar RNA polyadenylation and polyadenylate viral RNA (Chen et al., 2013). We investigated PAL of BaMV gRNA and sgRNA and found that the PAL of BaMV ranged from 150 to 300 nt, with median lengths of 144.84 nt (gRNA), 133.79 nt (TGBsgRNA), 148.95 nt (sgRNA2), and 100.90 nt (CPsgRNA), all substantially longer than those of host transcripts (Figures 7D and 5A). CPsgRNA, which encodes the coat protein and is highly expressed (Lima et al., 2017), showed the shortest PAL.

Some viral polymerases of RNA viruses (e.g., influenza A virus and Lassa virus) cleave the 5′UTR region of the host transcript to obtain a functional upstream start codon (uAUG) through a "cap-grabbing" process to generate chimeric host–viral RNA (Ho et al., 2020). RNA-seq identified virus–host chimeric RNAs (Zhang et al., 2020). Upon aligning long DRS reads to a combined reference sequence of the BaMV genome and *D. latiflorus* transcriptome, we identified a subset of potential chimeric reads that spanned both the BaMV and bamboo annotated transcripts, indicating their dual-origin alignment. After filtering out reads with mismatched orientations or <50 nt aligned on either end, we observed a clustering of junction sites near the start of CPsgRNA (5494 nt) (Figure 7e). Most host genes including fusion sites were downregulated after BaMV infection, which suggested that chimeric RNA formation might decrease host transcript abundance (Figure 7f). Genes with 6–7 chimeric sites showed reduced expression, and higher expressed genes generally had more chimeric sites, but this pattern was not seen at the protein level (Figure 7g). These findings hint at possible BaMV-*D. latiflorus* chimeric RNAs.

DISCUSSION

Posttranscriptional modifications on viral RNA are involved in viral replication cycles and host antiviral mechanisms (Wang et al., 2023). DRS sequencing identified at least 41 m^6A modification sites on SARS-CoV-2 RNA (Kim, Lee, Yang, et al., 2020), highlighting its precision in viral RNA methylation analysis. Building on these foundational work, we infected *D. latiflorus* with BaMV and identified 122 potential m^6A modification sites on viral RNA. Notably, the most common motif was AAACA, and we further discovered a certain degree of preference for the AAACC motif in CPsgRNA. For follow-up research, the causal relationship between m^6A modification sites and BaMV adaptability (such as viral replication and pathogenicity), especially the consensus modification sites in the overlapping regions of BaMV's gRNA and sgRNAs, can be validated by integrating site-directed mutagenesis. This will provide a new perspective for elucidating the molecular mechanism and plant virus–host interaction of BaMV infection in bamboo.

Since ONT data does not require reverse transcription or amplification and can span long sequences, it can be used to detect viral RNA chimerism. We found a small number of virus–host chimeric reads in ONT data, with chimeric sites in viral RNA enriched near the transcription start site of CPsgRNA. The generation of chimeric transcripts via viral "cap-snatching" relies on two hypotheses: (1) the host sequence cleaved by the virus contains an upstream AUG (uAUG) that can initiate translation; (2) the 5′ mRNA transcribed from the viral UTR lacks a stop codon (Ho et al., 2020). Therefore, further analysis of the distribution characteristics of chimeric sites in bamboo transcripts is needed, along with identification of whether the 5′ host sequence of chimeric reads contains uAUG or the 5′ viral sequence contains stop codons. Additionally, predicting open reading frames (ORFs) of chimeric reads and searching proteomics data can reveal whether chimeric proteins are produced. In summary, the existence and fusion mechanism of BaMV-bamboo chimeric RNAs require further exploration.

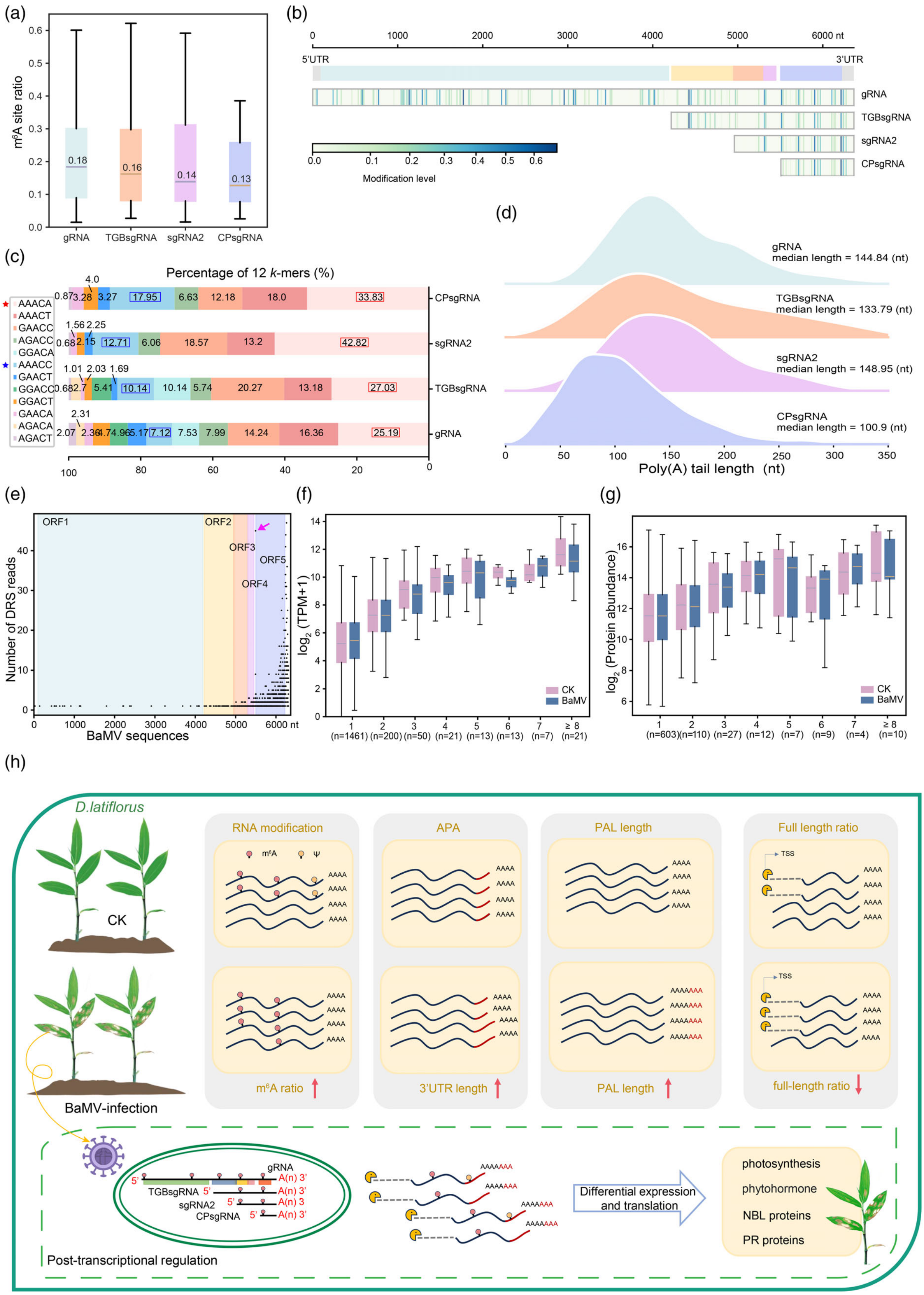
(a)
m6A site ratio
0.18
0.16
0.14
0.13
gRNA
TGBsgRNA
sgRNA2
CPsgRNA
(b)
0
1000
2000
3000
4000
5000
6000 nt
5'UTR
3'UTR
gRNA
TGBsgRNA
sgRNA2
CPsgRNA
Modification level
(c)
Percentage of 12 k-mers (%)
AAACA
AAACT
GAACC
AGACC
GGACA
AAACC
GAACT
GGACC
GGACT
GAACA
AGACA
AGACT
CPsgRNA
sgRNA2
TGBsgRNA
gRNA
(d)
gRNA
median length = 144.84 (nt)
TGBsgRNA
median length = 133.79 (nt)
sgRNA2
median length = 148.95 (nt)
CPsgRNA
median length = 100.9 (nt)
Poly(A) tail length (nt)
(e)
ORF1
ORF2
ORF3
ORF4
ORF5
Number of DRS reads
BaMV sequences
(f)
log2 (TPM+1)
CK
BaMV
(n=1461) (n=200) (n=50) (n=21) (n=13) (n=13) (n=7) (n=21)
(g)
log2 (Protein abundance)
CK
BaMV
(n=603) (n=110) (n=27) (n=12) (n=7) (n=9) (n=4) (n=10)
(h)
D.latiflorus
CK
BaMV-infection
RNA modification
m6A ratio
APA
3'UTR length
PAL length
PAL length
Full length ratio
full-length ratio
gRNA
TGBsgRNA
sgRNA2
CPsgRNA
Differential expression and translation
photosynthesis
phytohormone
NBL proteins
PR proteins
Post-transcriptional regulation

Figure 7. m^6A modification landscape and PAL features of BaMV.
(a) Box plots of m^6A modification ratio across BaMV RNAs.
(b) Heatmap of m^6A site distribution and levels in different RNA types.
(c) Histogram of m^6A motif usage frequencies.
(d) Ridge plot of poly(A) tail length distributions for BaMV.
(e) Scatterplot of coverage at potential fusion sites.
(f, g) Box plots of expression (f) and protein changes (g) associated with fusion site numbers.
(h) Model of RNA modification and posttranscriptional regulation in BaMV-*D. latiflorus* interactions.

Proteomic analysis of differential protein accumulation in virus-susceptible hosts provides critical insights into how viruses evade host immunity and whether plants can restrict viral infection. In this study, BaMV infection induced the downregulation of specific CNL and PR proteins, whereas no significant protein downregulation was observed in the RNAi component (Figure S28). In future, these antiviral proteins can be regarded as potential susceptibility factors that help the virus evade or suppress host immunity for further experimental validation. In our proteomic data, BaMV causes a decrease in the abundance of LHC and OEC in the photochemical reaction system. In the protein–protein interaction (PPI) network of DEPs, we observed reprogramming of metabolic processes beyond photosynthesis, including starch metabolism, protein translation and transport, protein repair, and glutamine synthesis. Notably, APR1, a key hub connecting sulfur metabolism, nitrogen metabolism, protein repair, and photosynthesis, may represent a critical gene for the host's multilayered metabolic responses to viral infection (e.g., antioxidant defense, damaged cell repair, and energy conversion). It could also serve as a potential susceptibility factor. Overall, changes in differential protein accumulation indicate that BaMV infection triggers widespread metabolic reprogramming and a series of pathological processes in *D. latiflorus*. The shifts in protein abundance are likely governed by precise posttranscriptional regulation, accompanied by coordinated changes at the transcriptional and protein levels.

We used Pearson Correlation Coefficient (Cor_p) to describe changes in the correlation between transcription and protein. In most tissues of Arabidopsis, transcription and protein levels exhibit positive correlations (Pearson correlation $r = 0.28–0.7$) (Mergner et al., 2020). In this study, the Cor_p values between transcriptional and protein abundances were approximately 0.2 in both full-length and non-full-length reads, with viral infection causing a downward trend in transcription–protein correlation. Intact transcripts are known to enhance translation efficiency, while 5′-truncated transcripts may be sequestered by viral mRNAs after ribosome release due to their low translation efficiency. In this study, BaMV infection led to a downregulation of the proportion of full-length of the host, which was not conducive to efficient translation of *D. latiflorus*. Furthermore, the upregulated full-length ratio and expression of splicing factors suggested BaMV may affect AS. Leveraging the length advantage of the DRS reads to identify AS events, we observed the greatest reduction in A3SS events. Notably, the presence of BaMV RNA consumed a portion of the sequencing reads, which consequently reduced the number of long reads mapping to the host *D. latiflorus* genome in the BaMV samples by 348 632 compared to the CK control. To mitigate this disparity in initial read counts, we normalized the reads by randomly down-sampling the CK sample to match the number of host-mapped reads in BaMV samples. Subsequent analysis of AS events revealed a shift in AS proportions (Figure S29). These results highlight that disparities in read counts can confound AS analysis by introducing sample-specific biases. Therefore, the AS results presented in this study should be tentatively considered preliminary qualitative conclusions.

In recent years, studies have revealed that viruses influence host physiology and pathology by remodeling the host epitranscriptome, with m^6A modification being the most prominent example (Lichinchi et al., 2016). Nanopore DRS technology provides a favorable tool for isoform-level identification and quantification of RNA modifications. In this study, we performed high-resolution identification of m^6A and Ψ modification sites in the transcripts of *D. latiflorus* after BaMV infection and characterized the distribution of the two modifications on the transcripts. Similar to the m^6A dynamics of rice after RBSDV and RSV infection, BaMV infection caused an increase in the overall m^6A level of host genes (Zhang et al., 2021), and there were hundreds of genes with the acquisition and loss of modification sites. These changes suggest that viral infection may alter the expression or protein abundance of m^6A "writers" and "erasers." Notably, we found that the protein abundance of *WTAP_C1* was significantly elevated after BaMV infection. While previous studies have shown that overexpression of *SlHAKAI* negatively regulates pepino mosaic virus (PepMV) infection, leading to delayed symptom development and milder mosaic phenotypes in tomato plants (He et al., 2023), the role of WTAP in viral infection remains uncharacterized. Future studies could employ overexpression or knockout approaches to investigate how WTAP affects viral accumulation and mosaic symptoms. Consistent with prior findings that m^6A modification levels are negatively correlated with gene expression and translation output, we confirmed this relationship in the context of viral infection by linking methylation changes to corresponding transcript and protein abundance changes. Similar trends were observed between virus-specific and constitutive modification genes, further supporting the regulatory role of epitranscriptomic remodeling in BaMV-bamboo interactions.

By integrating transcriptional and proteomic analyses, we observed that BaMV infection activated multiple host immune and defense genes involved in virus–host interactions, including CNL genes recognizing viral effectors (Figure S11a), RNAi components (Figure S28), PR family genes (Figure S22), and hormone regulatory genes (e.g., ABA, JA, and SA pathways) (Figure 3l, Figure S30 and Figure S31). Previous studies have shown that knocking down *NbABA1* and mutant *nced3* in the ABA synthesis pathway reduces BaMV titers (Alazem et al., 2014). In this study, *DlaNCED1* exhibited increased m^{6}A modification but impaired gene expression, suggesting that m^{6}A of *DlaNCED1* may negatively regulate BaMV accumulation, an observation requiring further experimental validation. Additionally, differentially m^{6}A-modified genes MgPME cyclase and *POR*, which are critical for chlorophyll synthesis, and the glutathione peroxidase (*GPx*) gene, associated with chlorophyll degradation, all showed upregulated modification but downregulated expression. This pattern implies a potential link among m^{6}A modification, gene expression, and pathological phenotypes.

Eukaryotic 3′-end processing is critical for gene expression and translational regulation. BaMV infection globally induced the usage of distal poly(A) sites in host. Changes in the concentration of 3′-end processing factors are one of the causes of dynamic APA changes. In this study, the protein abundance of PABPN1, which induced distal PAS usage in human cells, was significantly increased upon BaMV infection. 3′UTR length variations impact mRNA stability and translation efficiency. We correlated differential APA events with DEPs and observed that APA had impact on translational components (Table S12). However, how virus-induced APA changes specifically regulate the abundance of these proteins requires further exploration. This process may involve multiple regulatory mechanisms, such as changes in microRNA binding sites or RNA-binding protein (RBP)-mediated regulation.

Viral infection-induced changes in host energy metabolism and substance synthesis may indirectly influence cellular PAL lengths. This study demonstrated that BaMV infection led to global PAL elongation in bamboo, particularly in PR genes closely associated with viral invasion. PAL length is regulated by deadenylation mechanisms. Previous studies have shown that YTHDF recruits the CCR4-NOT deadenylase complex to promote the degradation of m^{6}A-modified mRNAs (Burgess et al., 2023), illustrating the impact of RNA modifications on PAL length. We analyzed the distribution of RNA modifications (m^{6}A and Ψ) on transcripts with altered PAL lengths and found that these transcripts preferentially acquired RNA modifications in the 3′UTR region after viral infection, particularly Ψ modifications.

The regulatory mechanisms of RNA are extremely complex, with some transcripts being finely coordinated by multilayered posttranscriptional regulatory factors. For example, viral infection upregulates cytoplasmic polyadenylation element-binding protein 1 (CPEB1), leading to shorter 3′UTRs and longer PALs in cellular genes (Batra et al., 2016). We established correlations between various posttranscriptional regulatory factors and changes at the transcript and protein levels, and found that a small number of transcripts were regulated by multiple factors, such as the JAZ gene was regulated by both m^{6}A and PAL. However, whether the regulation of the mRNA life cycle by BaMV infection is subject to the dynamic equilibrium of the synergistic effect of multiple factors still needs to be further experimentally verified and further studied.

In summary, we utilized Nanopore DRS technology to profile the epitranscriptomic modifications of BaMV and combined TMT-labeled proteomics to investigate posttranscriptional regulatory and proteomic changes in *D. latiflorus* leaf tissues in response to BaMV infection. Posttranscriptional regulators included m^{6}A modification, pseudouridylation (Ψ), poly(A) tail length, and 3′UTR length variations via APA (Figure 7h). Our results showed that BaMV RNA underwent m^{6}A methylation, and BaMV infection altered the translational output of various host posttranscriptional regulatory proteins. We also explored the potential association of posttranscriptional regulators with the expression of genes related to metabolic processes or symptom development, and with their corresponding protein abundance. This study further clarifies the impact of BaMV on *D. latiflorus*, and our findings may draw attention to the potential RNA modification and posttranscriptional regulation underlying plant virus-host interactions.

MATERIALS AND METHODS

BaMV infection and sample collection

BaMV vector from our previous study (Jin et al., 2023) was used to enrich BaMV in *DCL2/4* silenced *Nicotiana benthamiana* via Agrobacterium infiltration to inoculate 14-day-old *D. latiflorus* seedlings (CK and BaMV). After 30-day cultivation, successful infection was confirmed by leaf mosaic symptoms. Samples with three replicates per group were snap-frozen in liquid nitrogen and stored at −80°C for subsequent DRS, liquid chromatography-tandem mass spectrometer (LC–MS/MS), and RNA-seq.

RNA extraction, library construction, and analysis for DRS

Total RNA was extracted from samples (CK and BaMV) using the RNAprep Pure Kit (Code no. DP441; Tiangen Co. Ltd, Beijing, China) following the manufacturer's protocol. DNase I treatment was subsequently applied to eliminate DNA contamination. Poly(A) + RNA was isolated from two biological replicates per group using the Dynabeads™ mRNA Purification Kit (Code no. 61006; Thermo Scientific Co. Ltd, Springs, CO, USA). After preliminary quality assessment, the DRS library was constructed according to the protocol of the SQK-RNA002 Kit from Oxford Nanopore Technologies. The purified poly(A) + RNA was ligated to the ONT Reverse Transcription Adapter (RTA) using concentrated T4 DNA Ligase (Code no. M0202; NEB Co. Ltd, Ipswich, MA, USA) and then reverse transcribed using SuperScript III Reverse Transcriptase (Code no. 18080093; Thermo Fisher Scientific Co. Ltd, CO) for first-strand cDNA synthesis. Each library was sequenced on a MinION device equipped with a FLO-MIN106 (ONT R9.4) flow cell, utilizing standard MinKNOW software.

The raw current signals (in FAST5 format) was performed basecalling for Guppy (v3.6.1) with following parameters: --flowcell FLO-MIN106 --kit SQK-RNA002, which were then converted to FASTA format and corrected using LoRDEC (- k 19 -s 3) (Salmela & Rivals, 2014) with Illumina short reads. The corrected reads were mapped to the BaMV reference sequences (Jin et al., 2023) and *D. latiflorus* genomes (Zheng et al., 2022), respectively, using minimap2 (Li, 2018) with the parameters: -ax map-ont -uf. The number of reads was counted using featureCounts (-L -R CORE -t transcript) (Liao et al., 2014) and then normalized by RPM to represent expression levels.

Identification of DEGs based on short reads

Sequencing libraries were constructed from three biological replicates per group (CK and BaMV) and sequenced on an Illumina Novaseq 6000 instrument (Berry Genomics Co. Ltd, Beijing, China). Raw reads were preprocessed using fastp (Chen, Zhou, et al., 2018) to trim adapter sequences and filter low-quality bases. Cleaned reads were aligned separately to the *D. latiflorus* and BaMV reference genome using HISAT2 (Kim et al., 2019) with default parameters, and alignment outputs were converted to BAM format. Reads with unique mapping positions were retained for downstream analysis. Gene-level read counts were quantified using featureCounts, and expression values were normalized to TPM to construct the expression matrix. Differential expression analysis was performed using the DESeq2 R package (Love et al., 2014). *P*-values were adjusted with the "Benjamini–Hochberg" method to control the false discovery rate (FDR), and genes with *P*.adjust <0.05 and absolute fold change >1.5 were defined as significantly DEGs.

Identification of full length and non-full length reads

Corrected DRS reads were classified as full-length or non-full-length based on whether their 5′ mapping start sites were located within 20 nucleotides downstream of the annotated translation start site. For each gene in both CK and BaMV, the full-length read ratio was calculated as: full-length reads/total reads. Fisher's exact test was applied to compare the distribution of full-length and non-full-length reads between groups, with $P < 0.05$ used as the threshold to identify genes with significantly altered full-length ratios.

AS events identification and differential splicing event quantification

BAM files aligned to the *D. latiflorus* genome were used for transcript isoform assembly with StringTie in long-read mode (Pertea et al., 2015). SUPPA2 (Trincado et al., 2018) was employed to identify AS events and subsequent differential splicing analysis. Specifically, after quantifying the assembled transcripts using next-generation RNA-seq data, we used the psiPerEvent module of SUPPA2 to calculate Percent Spliced In (PSI) values, which represent the relative abundance of AS isoforms. Genes with |dPSI| >1 and $P < 0.05$ were identified as differentially spliced genes using the diffSplice module of SUPPA2.

Prediction of m^{6}A modification sites and identification of DE m^{6}A on transcripts

Firstly, multi-read FAST5 files were split into single-read FAST5 levels using multi_to_single_fast5 module from guppy. The resquiggle algorithm from Tombo (Love et al., 2014) was then used to map raw signal data to the host transcriptome and BaMV genome. Finally, Nanom6A (Gao et al., 2021) was applied to detect m^{6}A sites based on signal features, with the parameter "--support 10" for the least modified reads per site. For each site, the m^{6}A modification ratio was calculated as: modified reads/(modified + unmodified reads). Modified sites with $P < 0.05$ (Fisher's exact test) and the ratio difference across groups >0.1 were considered as differential m^{6}A.

Prediction of Ψ sites at single-base resolution

We used NanoSPA to detect pseudouridine (Ψ) modification sites (Huang et al., 2024). Following the NanoSPA workflow, raw FASTQ reads were aligned to *D. latiflorus* genome using "nanospa alignment." Spliced reads were processed with "nanospa remove_intron" to remove signal padding over intronic regions. Base-level features were then extracted using "nanospa extract_features," and only sites covered by at least 20 reads were retained for downstream analysis. Finally, module "prediction_psU" was used to predict Ψ modification probabilities for each uridine (U) site. Sites with a predicted modification probability ≥0.8 were considered pseudouridylated.

Estimation of PAL and APA based on 3′UTR length variations

PAL of each read was estimated using the polya module in nanopolish (v0.13.2) with parameters: --threads = 40 (Workman et al., 2019). Retaining only reads with both "Assigned" status from featureCounts (using parameters: -L -R CORE) in long-read mode and QC labeled as "PASS" from nanopolish for downstream analysis, gene-level PALs were calculated as the median PAL of all reads assigned to each gene. Differential PALs between CK and BaMV were identified using the Mann–Whitney *U* test, with significance thresholds set at $P < 0.05$ and fold change >1.5.

The 3′ end positions of retained reads mentioned above were defined as polyadenylation sites (PASs) for APA analysis as previous method (Li et al., 2023). PASs within 24 nt were clustered, with each PAS supported by at least three reads. The most abundant PAS in each cluster was designated as the representative PAS. Genes with fewer than five supporting reads were excluded. The top two PASs from per gene were selected and classified as distal (dPAS) or proximal (pPAS) based on their positions along the transcript. Genes with a relative expression difference (RED), calculated as $|\log_2[\mathrm{dPAS_{BaMV}}/\mathrm{dPAS_{CK}}] - \log_2[\mathrm{pPAS_{BaMV}}/\mathrm{pPAS_{CK}}]|$, greater than 30% were considered to exhibit significant 3′UTR length changes.

GO and KEGG enrichment analysis

Functional annotation of *D. latiflorus* was performed using Blast2GO. GO and KEGG enrichment analyses were conducted using the R package clusterProfiler (v4.6.2). Terms with $P < 0.05$ were considered significant.

Protein extraction, digestion, and TMT labeling

Frozen leaf samples (three biological replicates for CK and BaMV) were ground in liquid nitrogen. A total of 0.3 g of powdered tissue was lysed in 1 ml of buffer containing 10 mM Tris–HCl (pH 8.0), 5 mM EDTA, 1% SDS, 8 M urea, and 20 mM DTT. After vortexing, samples were incubated on ice for 30 min with mixing every 5 min, followed by vertical rotation at 4°C for 2 h (20 rpm). Lysates were centrifuged at 15 000 rpm for 30 min at 4°C; supernatants were clarified by a second centrifugation and proteins were precipitated overnight at −20°C with six volumes of 10% TCA/acetone. Precipitates were washed twice with cold acetone, air-dried, and dissolved in urea buffer (8 M urea, 25× protease inhibitor cocktail, 100 mM Tris–HCl, pH 8.0). After final centrifugation, protein concentration was quantified using the BCA assay and SDS-PAGE was performed.

Protein digestion was performed using a modified filter-aided sample preparation (FASP) protocol (Wiśniewski et al., 2009). For each biological replicate, 100 μg of protein was mixed with 8 M urea to ensure a final concentration >4 M, followed by the addition of 1 M DTT to a final concentration of 20 mM. Samples were incubated at 37°C for 1 h. Subsequently, 1 M iodoacetamide (IAA) was added to a final concentration of 50–60 mM and incubated in the dark at room temperature for 30 min. The mixtures were centrifuged at 12 000 rpm for 10 min. The retentate was washed twice with 100 μl of 8 M urea and centrifuged under the same conditions. Then, 100 μl of 50 mM ammonium bicarbonate (ABC) or triethylammonium bicarbonate (TEAB) was added and centrifuged again; this step was repeated 2–5 times. After buffer exchange, samples were transferred to new collection tubes and digested with trypsin at a 1:50 (enzyme: protein, w/w) ratio in 100 μl digestion buffer at 37°C for at least 8 h. After digestion, samples were briefly vortexed and centrifuged at 12 000 rpm for 10 min. An additional 100 μl of HPLC-grade water was added, followed by another centrifugation. The resulting filtrates were vacuum-dried and stored at −20°C for further analysis.

Peptide mixtures were labeled with tandem mass tag (TMT) reagents (Thermo Fisher Scientific) at a 10:1 reagent-to-peptide ratio, according to the manufacturer's instructions. Labeled peptides were pre-fractionated using an Ultimate 3000 system (Thermo Fisher Scientific), and mass spectrometry using liquid chromatography–tandem mass spectrometry (LC–MS/MS) on Orbitrap Fusion Lumos mass spectrometer was performed as our previous method (Yu et al., 2019).

LC–MS/MS data analysis

Raw mass spectrometry data were searched against the annotated *D. latiflorus* protein database using Proteome Discoverer, with redundant sequences removed. The search parameters were set as follows: a precursor ion mass tolerance of 10 ppm and a fragment ion mass tolerance of 0.02 Da. Trypsin was specified as the proteolytic enzyme, allowing up to two missed cleavages. Fixed modifications included carbamidomethylation of cysteine and TMT10 labeling on peptide N-termini. Variable modifications included methionine oxidation and N-terminal acetylation. A FDR of <1% at the peptide level and at least one unique peptide per protein were required for protein identification. For quantification, only nonredundant unique peptides with a signal-to-noise (S/N) ratio >1.5 and FDR <0.05 were included. Reporter ion intensities were normalized across channels based on the summed total intensity to account for sample loading differences. DEPs were identified using a fold change threshold >1.5 and $P < 0.05$ determined by t-test.

Construction of protein–protein interaction network

Protein sequences of rice (*O. sativa* IRGSP-1.0.57) were downloaded from the Ensembl Plants database (https://plants.ensembl.org). Homologous protein pairs between *D. latiflorus* and rice were identified using InParanoid (Ostlund et al., 2010). Rice homologs corresponding to DEPs in *D. latiflorus* were input into the STRING database for interaction prediction, with a minimum interaction score threshold of 0.6. Disconnected nodes were removed, and the remaining proteins were clustered using the Markov Cluster (MCL) algorithm. The interaction network was visualized in Cytoscape based on the interaction score matrix. Key hub proteins were identified using the cytoHubba plugin with the Betweenness centrality algorithm, and the top 10 nodes were selected as key interacting proteins.

AUTHOR CONTRIBUTIONS

L.G. conceived this project and designed the experiments. XL., JZ., ZZ., YW., HW., WL., and HZ., performed bioinformatics analysis. LW., HW., XJ., RW., and LZ carried out the experiments. XL. and L.G. wrote the manuscript. All authors contributed to the article and approved the submitted version.

ACKNOWLEDGMENTS

We acknowledge the technical support from Instrumental Analysis Center of Fujian Agriculture and Forestry University for TMT-based proteomic experiments. We sincerely thank Mingchuan Bao, Yandong Jin, and Baijie Wang for their assistance in BaMV treatment and sample collection. This research was funded by the National Key R&D Program of China (2021YFD2200505), the National Natural Science Foundation of China (32371980), the Natural Science Foundation of Fujian Province (2025J02014), the S&T Innovation (KFB23180 and KFB24096A), and the Forestry Peak Discipline Construction Project of Fujian Agriculture and Forestry University (725025010 and 72202200205).

ACCESSION NUMBER

Raw ONT FAST5 sequencing data has been submitted to National Genomics Data Center (NGDC) under accession number CRA019442 of PRJCA030548. Mass spectrometry proteomics data were available at ProteomeXchange Consortium (Deutsch et al., 2022) with the dataset identifier PXD061707. The genomic sequencing and annotation files of *D. latiflorus* were unveiled at https://doi.org/10.6084/m9.figshare.24411913.v3. The analyze codes are available at https://github.com/q123-sketch/BaMV-Dendrocalamus-latiflorus-interactions.

CONFLICT OF INTEREST

The authors declare that they have no competing interests.

DATA AVAILABILITY STATEMENT

Raw ONT FAST5 sequencing data has been submitted to National Genomics Data Center (NGDC) under accession number CRA019442 of PRJCA030548. Mass spectrometry proteomics data were available at ProteomeXchange Consortium (Deutsch et al., 2022) with the dataset identifier PXD061707. The genomic sequencing and annotation files of *D. latiflorus* were unveiled at https://doi.org/10.6084/m9.figshare.24411913.v3. The analyze codes are available at https://github.com/q123-sketch/BaMV-Dendrocalamus-latiflorus-interactions.

SUPPORTING INFORMATION

Additional Supporting Information may be found in the online version of this article.

Figure S1. Scatterplot showing differential expression for genes with differential full-length ratios.

Figure S2. Lollipop plots showing GO enrichment analysis of genes with decreased full-length transcript ratios.

Figure S3. Histogram showing the number of genes detected AS events (A) and UpSet plot depicting number of isoforms formed by various AS events (B).

Figure S4. Lollipop plots showing GO enrichment analysis of upregulated proteins.

Figure S5. Density plots showing the $\log_{10}$-transformed ratios of transcriptional to protein fold changes for (A) 6944 matched genes, (B) 5550 unchanged genes, and (C) 1394 differentially expressed genes.

Figure S6. Frequency distribution of (A) full-length RNA abundance (RPM), (B) non-full-length RNA abundance (RPM), and (C) protein abundance across all samples.

Figure S7. Dumbbell plot presenting Cor_p of gene clusters in full-length reads according to KEGG terms.

Figure S8. Dumbbell plot presenting Cor_p of gene clusters in non-full length reads according to KEGG terms.

Figure S9. Cor_p of “class I fructose-bisphosphate aldolase” pathway in full-length reads (A) and non-full-length reads (B) across the CK and BaMV groups.

Figure S10. Wiggle plots visualizing the m^6A sites of four m^6A regulators.

Figure S11. Associations between m^6A modifications and expression patterns of CNL genes. (A) Raincloud plots showing changes in transcriptional and protein abundances of CNL genes. (B) The box diagram shows the RPM expression levels of 14 m^6A-modified CNL genes, which are divided into high and low modification genes according to the modification levels of the CK group. (C) The histogram depicting changes in the distribution proportion of m^6A modification sites on CNL mRNA.

Figure S12. The ridge plot shows the expression distribution of m6A-specific modification genes with an RPM value of >0. (A, B) Gene expression level distributions for CMGs and SMGs in the CK and BaMV groups. (C) Distribution patterns of modification sites. (D) Bar chart showing fold changes in expression levels of autophagy-related genes.

Figure S13. GO enrichment analysis of genes harboring the GGACA motif among those with significantly decreased m^6A modification levels.

Figure S14. GO enrichment analysis of genes with significantly upregulated (A) or downregulated (B) modifications following BaMV infection.

Figure S15. Wiggle plot showing the distribution and modification ratio of m^6A modified *CYP71A19*.

Figure S16. Qualitative analysis of Ψ sites in *D. latiflorus* transcripts affected by BaMV infection. (A) Venn diagram showing the number of predicted Ψ sites in the CK and BaMV groups, respectively. (B) Density plot illustrating the distribution of pseudouridine sites on mRNA. (C) The number of transcripts with varying numbers of m^6A and pseudouridine modification sites in the CK and BaMV groups. (D) Box plot illustrating the expression levels of genes with two types of modifications simultaneously and those with only one type of modification. (E) Distribution of the relative distances between m^6A modification sites and Ψ sites, compared to random sites, on each transcript. The *x*-axis values were normalized to the range $[-1,1]$ based on the distance.

Figure S17. GO enrichment analysis of transcripts with specific Ψ modifications in the BaMV group.

Figure S18. Changes in m^6A modification ratios, PAL values, mRNA expression levels, and protein abundances of APA regulatory factors under viral infection. The Y-axis labels are colored to denote different factor categories: cleavage and polyadenylation specificity factor (CPSF) complex, cleavage stimulation factor (CSTF) complex, cleavage factor Im (CFIm) complex, cleavage factor IIm (CFIIm) complex, and auxiliary protein monomers.

Figure S19. GO enrichment analysis was performed using genes at the distal poly(A) sites (A) and the proximal poly(A) sites (B) after viral infection.

Figure S20. The Wiggle plot showed the gene involved in transcription corepressor selecting proximal poly(A) sites, the histograms showed the changes in the ratio of dPAS to pPAS, and the changes in expression level and protein abundance after viral infection, respectively.

Figure S21. The number of different types of PR genes identified in *D. latiflorus*.

Figure S22. Box plots depicting overall alterations in m^6A modification rates, expression levels, and protein abundances of distinct PR gene subtypes following BaMV infection.

Figure S23. Box plots showing genes with significantly elongated (A) or shortened (B) PAL induced by viral infection.

Figure S24. GO enrichment analysis was performed for the genes that significantly lengthened PAL (A) and shortened (B) after viral infection. The top 20 entries of biological process (BP), molecular fun-ction (MF), and cellular composition (CC) were displayed.

Figure S25. Scatterplot showing the correlation between expression and full-length ratio.

Figure S26. The pie charts showing the association of posttranscriptional regulators in response to viral infection with DEGs and DEPs.

Figure S27. KEGG pathway analysis of factors-related and -unrelated transcripts identified in Figure 6d, with the top five entries displayed, respectively.

Figure S28. Changes in m^6A modification rates, PAL, expression levels, and protein abundances of AGO (gray), DCL (yellow), and RDR (blue) families in the RNAi silencing pathway under BaMV infection.

Figure S29. Bar plot showing the number of different AS events across different samples.

Figure S30. Changes in m^6A modification ratios, PAL, 3′UTR lengths, expression levels, and protein abundances of genes involved in jasmonic acid synthesis (gray), transcription factors (yellow), and regulatory factors (blue) following BaMV infection.

Figure S31. Changes in m^6A modification ratios, PAL, 3′UTR lengths, expression levels, and protein abundances of genes involved in the salicylic acid synthesis pathway (gray), transcription factors (yellow), and regulatory factors (blue) after BaMV infection.

Table S1. List of significant changes of full-length ratio in BaMV versus CK.

Table S2. DE proteins in BaMV versus CK.

Table S3. Differential proteins in proteins related to photosynthesis, PR genes, and CNL genes.

Table S4. Node pairing of rice-bamboos in the PPI network.

Table S5. DE genes in BaMV versus CK.

Table S6. List of m^6A regulators, APA regulators, hormone regulators, PR genes, and CNL genes.

Table S7. Transcript and protein level changes of CNL-type genes.

Table S8. DE m^6A modified sites in BaMV versus CK.

Table S9. DE m^6A genes versus DEGs and DEPs in BaMV versus CK.

Table S10. Ψ specific modified sites between CK and BaMV.

Table S11. Differential 3′UTR length in BaMV versus CK.

Table S12. The changes in protein abundance of differential APA genes and the mean m^6A modification ratios of genes with differential APA in the 3′UTR region.

Table S13. Changes in gene expression and protein abundance of differential PAL genes.

Table S14. A list of genes that are regulated by different types of factor in each change.

Table S15. KEGG enrichment analysis of multifactor-regulated transcripts and proteins under viral infection.

Table S16. List of modified motif and PAL for reads assigned to different types of RNA.

Table S17. List of BaMV sequence.

REFERENCES

Alazem, M., **Lin, K.Y.** & **Lin, N.S.** (2014) The abscisic acid pathway has multifaceted effects on the accumulation of bamboo mosaic virus. *Molecular Plant-Microbe Interactions*, **27**, 177–189.

Batra, R., **Stark, T.J.**, **Clark, A.E.**, **Belzile, J.-P.**, **Wheeler, E.C.**, **Yee, B.A.** ***et al.*** (2016) RNA-binding protein CPEB1 remodels host and viral RNA landscapes. *Nature Structural & Molecular Biology*, **23**, 1101–1110.

Burgess, H.M., **Grande, R.**, **Riccio, S.**, **Dinesh, I.**, **Winkler, G.S.**, **Depledge, D.P.** ***et al.*** (2023) CCR4-NOT differentially controls host versus virus poly(a)-tail length and regulates HCMV infection. *EMBO Reports*, **24**, e56327.

Campos, C.M., **Tsai, K.**, **Courtney, D.G.**, **Bogerd, H.P.**, **Holley, C.L.** & **Cullen, B.R.** (2021) Mapping of pseudouridine residues on cellular and viral transcripts using a novel antibody-based technique. *RNA (New York, N.Y.)*, **27**, 1400–1411.

Chang, H., **Lim, J.**, **Ha, M.** & **Kim, V.N.** (2014) TAIL-seq: genome-wide determination of poly(a) tail length and 3′ end modifications. *Molecular Cell*, **53**, 1044–1052.

Chen, I.H., **Chen, H.T.**, **Huang, Y.P.**, **Huang, H.C.**, **Shenkwen, L.L.**, **Hsu, Y.H.** ***et al.*** (2018) A thioredoxin NbTRXh2 from *Nicotiana benthamiana* negatively regulates the movement of bamboo mosaic virus. *Molecular Plant Pathology*, **19**, 405–417.

Chen, I.H., **Cheng, J.H.**, **Huang, Y.W.**, **Lin, N.S.**, **Hsu, Y.H.** & **Tsai, C.H.** (2013) Characterization of the polyadenylation activity in a replicase complex from bamboo mosaic virus-infected *Nicotiana benthamiana* plants. *Virology*, **444**, 64–70.

Chen, S., **Zhou, Y.**, **Chen, Y.** & **Gu, J.** (2018) Fastp: an ultra-fast all-in-one FASTQ preprocessor. *Bioinformatics*, **34**, i884–i890.

Cheng, C.P. & **Tsai, C.H.** (1999) Structural and functional analysis of the 3′ untranslated region of bamboo mosaic potexvirus genomic RNA. *Journal of Molecular Biology*, **288**, 555–565.

Colgan, D.F. & **Manley, J.L.** (1997) Mechanism and regulation of mRNA polyadenylation. *Genes & Development*, **11**, 2755–2766.

Cui, H., **Tsuda, K.** & **Parker, J.E.** (2015) Effector-triggered immunity: from pathogen perception to robust defense. *Annual Review of Plant Biology*, **66**, 487–511.

Deutsch, E.W., **Bandeira, N.**, **Perez-Riverol, Y.**, **Sharma, V.**, **Carver, J.J.**, **Mendoza, L.** ***et al.*** (2022) The ProteomeXchange consortium at 10 years: 2023 update. *Nucleic Acids Research*, **51**, D1539–D1548.

Engel, M., **Eggert, C.**, **Kaplick, P.M.**, **Eder, M.**, **Röh, S.**, **Tietze, L.** ***et al.*** (2018) The role of m(6)a/m-RNA methylation in stress response regulation. *Neuron*, **99**, 389–403.e389.

Floor, S.N. & **Doudna, J.A.** (2016) Tunable protein synthesis by transcript isoforms in human cells. *eLife*, **5**, e10921.

Gallegos, J. (2018) Alternative splicing plays a major role in plant response to cold temperatures. *Plant Cell*, **30**, 1378–1379.

Gao, Y., **Liu, X.**, **Jin, Y.**, **Wu, J.**, **Li, S.**, **Li, Y.** ***et al.*** (2022) Drought induces epitranscriptome and proteome changes in stem-differentiating xylem of *Populus trichocarpa*. *Plant Physiology*, **190**, 459–479.

Gao, Y., **Liu, X.**, **Wu, B.**, **Wang, H.**, **Xi, F.**, **Kohnen, M.V.** ***et al.*** (2021) Quantitative profiling of N(6)-methyladenosine at single-base resolution in stem-differentiating xylem of *Populus trichocarpa* using nanopore direct RNA sequencing. *Genome Biology*, **22**, 22.

Guo, Y. & **Gan, S.** (2006) AtNAP, a NAC family transcription factor, has an important role in leaf senescence. *The Plant Journal*, **46**, 601–612.

He, H., **Ge, L.**, **Li, Z.**, **Zhou, X.** & **Li, F.** (2023) Pepino mosaic virus antagonizes plant m(6)a modification by promoting the autophagic degradation of the m(6)a writer HAKAI. *aBIOTECH*, **4**, 83–96.

He, Y., **Li, L.**, **Yao, Y.**, **Li, Y.**, **Zhang, H.** & **Fan, M.** (2021) Transcriptome-wide N6-methyladenosine (m(6)a) methylation in watermelon under CGMMV infection. *BMC Plant Biology*, **21**, 516.

Ho, J.S.Y., **Angel, M.**, **Ma, Y.**, **Sloan, E.**, **Wang, G.**, **Martinez-Romero, C.** ***et al.*** (2020) Hybrid gene origination creates human-virus chimeric proteins during infection. *Cell*, **181**, 1502–1517.e1523.

Höller, K., **Király, L.**, **Künstler, A.**, **Müller, M.**, **Gullner, G.**, **Fattinger, M.** ***et al.*** (2010) Enhanced glutathione metabolism is correlated with sulfur-induced resistance in tobacco mosaic virus-infected genetically susceptible *Nicotiana tabacum* plants. *Molecular Plant-Microbe Interactions*, **23**, 1448–1459.

Hsu, Y.H. & **Lin, N.S.** (2004) Bamboo mosaic. In: Lapierre, H. & Signoret, P.A. (Eds.) *Viruses and virus disease of Poaceae (Gramineae)*. Paris: Institut National de la Recherche Agronomique, pp. 723–724.

Huang, S., **Wylder, A.C.** & **Pan, T.** (2024) Simultaneous nanopore profiling of mRNA m(6)a and pseudouridine reveals translation coordination. *Nature Biotechnology*, **42**, 1831–1835.

Huang, Y.W., **Sun, C.I.**, **Hu, C.C.**, **Tsai, C.H.**, **Meng, M.**, **Lin, N.S.** ***et al.*** (2021) NbPsbO1 interacts specifically with the bamboo mosaic virus (BaMV) subgenomic RNA (sgRNA) promoter and is required for efficient BaMV sgRNA transcription. *Journal of Virology*, **95**, e0083121.

Jenal, M., **Elkon, R.**, **Loayza-Puch, F.**, **van Haaften, G.**, **Kühn, U.**, **Menzies, F.M.** ***et al.*** (2012) The poly(a)-binding protein nuclear 1 suppresses alternative cleavage and polyadenylation sites. *Cell*, **149**, 538–553.

Jia, X., **Yuan, S.**, **Wang, Y.**, **Fu, Y.**, **Ge, Y.**, **Ge, Y.** ***et al.*** (2017) The role of alternative polyadenylation in the antiviral innate immune response. *Nature Communications*, **8**, 14605.

Jiang, B., **Su, C.**, **Wang, Y.**, **Xu, X.**, **Li, Y.** & **Ma, D.** (2023) Genome-wide identification of glutathione peroxidase (GPX) family genes and silencing TaGPX3.2A reduced disease resistance in wheat. *Plant Physiology and Biochemistry*, **204**, 108139.

Jin, Y., **Wang, B.**, **Bao, M.**, **Li, Y.**, **Xiao, S.**, **Wang, Y.** ***et al.*** (2023) Development of an efficient expression system with large cargo capacity for interrogation of gene function in bamboo based on bamboo mosaic virus. *Journal of Integrative Plant Biology*, **65**, 1369–1382.

Khanna-Chopra, R. (2012) Leaf senescence and abiotic stresses share reactive oxygen species-mediated chloroplast degradation. *Protoplasma*, **249**, 469–481.

Kierzek, E., **Malgowska, M.**, **Lisowiec, J.**, **Turner, D.H.**, **Gdaniec, Z.** & **Kierzek, R.** (2014) The contribution of pseudouridine to stabilities and structure of RNAs. *Nucleic Acids Research*, **42**, 3492–3501.

Kim, D., **Lee, J.Y.**, **Yang, J.S.**, **Kim, J.W.**, **Kim, V.N.** & **Chang, H.** (2020) The architecture of SARS-CoV-2 transcriptome. *Cell*, **181**, 914–921.e910.

Kim, D., **Lee, Y.S.**, **Jung, S.J.**, **Yeo, J.**, **Seo, J.J.**, **Lee, Y.Y.** ***et al.*** (2020) Viral hijacking of the TENT4-ZCCHC14 complex protects viral RNAs via mixed tailing. *Nature Structural & Molecular Biology*, **27**, 581–588.

Kim, D., **Paggi, J.M.**, **Park, C.**, **Bennett, C.** & **Salzberg, S.L.** (2019) Graph-based genome alignment and genotyping with HISAT2 and HISAT-genotype. *Nature Biotechnology*, **37**, 907–915.

Kogovšek, P., **Pompe-Novak, M.**, **Petek, M.**, **Fragner, L.**, **Weckwerth, W.** & **Gruden, K.** (2016) Primary metabolism, phenylpropanoids and antioxidant pathways are regulated in potato as a response to potato virus Y infection. *PLoS One*, **11**, e0146135.

Kuwabara, C., **Arakawa, K.** & **Yoshida, S.** (1999) Abscisic acid-induced secretory proteins in suspension-cultured cells of winter wheat. *Plant and Cell Physiology*, **40**, 184–191.

Lan, P., **Yeh, W.B.**, **Tsai, C.W.** & **Lin, N.S.** (2010) A unique glycine-rich motif at the N-terminal region of bamboo mosaic virus coat protein is required for symptom expression. *Molecular Plant-Microbe Interactions*, **23**, 903–914.

Lee, Y.S., **Lin, B.Y.**, **Hsu, Y.H.**, **Chang, B.Y.** & **Lin, N.S.** (1998) Subgenomic RNAs of bamboo mosaic potexvirus-V isolate are packaged into virions. *Journal of General Virology*, **79**(Pt 7), 1825–1832.

Li, A., **Chen, Y.S.**, **Ping, X.L.**, **Yang, X.**, **Xiao, W.**, **Yang, Y.** ***et al.*** (2017) Cytoplasmic m(6)A reader YTHDF3 promotes mRNA translation. *Cell Research*, **27**, 444–447.

Li, H. (2018) Minimap2: pairwise alignment for nucleotide sequences. *Bioinformatics*, **34**, 3094–3100.

Li, H., **Wang, G.**, **Ye, C.**, **Zou, Z.**, **Jiang, B.**, **Yang, F.** ***et al.*** (2025) Quantitative RNA pseudouridine maps reveal multilayered translation control through plant rRNA, tRNA and mRNA pseudouridylation. *Nature Plants*, **11**, 234–247.

Li, T., **Wang, H.**, **Zhang, Y.**, **Wang, H.**, **Zhang, Z.**, **Liu, X.** ***et al.*** (2023) Comprehensive profiling of epigenetic modifications in fast-growing Moso bamboo shoots. *Plant Physiology*, **191**, 1017–1035.

Li, X., **Zhu, P.**, **Ma, S.**, **Song, J.**, **Bai, J.**, **Sun, F.** ***et al.*** (2015) Chemical pull-down reveals dynamic pseudouridylation of the mammalian transcriptome. *Nature Chemical Biology*, **11**, 592–597.

Li, Y.J., **Chen, Y.J.**, **Hsu, Y.H.** & **Meng, M.** (2001) Characterization of the AdoMet-dependent guanylyltransferase activity that is associated with the N terminus of bamboo mosaic virus replicase. *Journal of Virology*, **75**, 782–788.

Liao, Y., **Smyth, G.K.** & **Shi, W.** (2014) featureCounts: an efficient general purpose program for assigning sequence reads to genomic features. *Bioinformatics*, **30**, 923–930.

Lichinchi, G., **Zhao, B.S.**, **Wu, Y.**, **Lu, Z.**, **Qin, Y.**, **He, C.** ***et al.*** (2016) Dynamics of human and viral RNA methylation during zika virus infection. *Cell Host & Microbe*, **20**, 666–673.

Lima, S.A., **Chipman, L.B.**, **Nicholson, A.L.**, **Chen, Y.H.**, **Yee, B.A.**, **Yeo, G.W.** ***et al.*** (2017) Short poly(a) tails are a conserved feature of highly expressed genes. *Nature Structural & Molecular Biology*, **24**, 1057–1063.

Lin, N.S., **Chai, Y.J.**, **Huang, T.Y.** & **Hsu, Y.H.** (1993) Incidence of bamboo mosaic potexvirus in Taiwan. *Plant Disease*, **77**, 450.

Lin, R. & **Wang, H.** (2004) Arabidopsis FHY3/FAR1 gene family and distinct roles of its members in light control of Arabidopsis development. *Plant Physiology*, **136**, 4010–4022.

Liu, J., **Yang, J.**, **Bi, H.** & **Zhang, P.** (2014) Why mosaic? Gene expression profiling of African cassava mosaic virus-infected cassava reveals the effect of chlorophyll degradation on symptom development. *Journal of Integrative Plant Biology*, **56**, 122–132.

Love, M.I., **Huber, W.** & **Anders, S.** (2014) Moderated estimation of fold change and dispersion for RNA-seq data with DESeq2. *Genome Biology*, **15**, 550.

Lu, M., **Zhang, Z.**, **Xue, M.**, **Zhao, B.S.**, **Harder, O.**, **Li, A.** ***et al.*** (2020) N(6)-methyladenosine modification enables viral RNA to escape recognition by RNA sensor RIG-I. *Nature Microbiology*, **5**, 584–598.

Mayr, C. (2016) Evolution and biological roles of alternative 3′UTRs. *Trends in Cell Biology*, **26**, 227–237.

Mayr, C. & **Bartel, D.P.** (2009) Widespread shortening of 3′UTRs by alternative cleavage and polyadenylation activates oncogenes in cancer cells. *Cell*, **138**, 673–684.

Mergner, J., **Frejno, M.**, **List, M.**, **Papacek, M.**, **Chen, X.**, **Chaudhary, A.** ***et al.*** (2020) Mass-spectrometry-based draft of the Arabidopsis proteome. *Nature*, **579**, 409–414.

Mulroney, L., **Wulf, M.G.**, **Schildkraut, I.**, **Tzertzinis, G.**, **Buswell, J.**, **Jain, M.** ***et al.*** (2022) Identification of high-confidence human poly(a) RNA isoform scaffolds using nanopore sequencing. *RNA*, **28**, 162–176.

Navrot, N., **Collin, V.r.**, **Gualberto, J.**, **Gelhaye, E.**, **Hirasawa, M.**, **Rey, P.** ***et al.*** (2006) Plant glutathione peroxidases are functional peroxiredoxins distributed in several subcellular compartments and regulated during biotic and abiotic stresses. *Plant Physiology*, **142**, 1364–1379.

Nelson, S. & **Borth, W.** (2011) *Bamboo mosaic*. Honolulu (HI): University of Hawaii, p. 4. (Plant Disease Series; PD-76).

Ostlund, G., **Schmitt, T.**, **Forslund, K.**, **Köstler, T.**, **Messina, D.N.**, **Roopra, S.** ***et al.*** (2010) InParanoid 7: new algorithms and tools for eukaryotic orthology analysis. *Nucleic Acids Research*, **38**, D196–D203.

Pascual, J., **Alegre, S.**, **Nagler, M.**, **Escandón, M.**, **Annacondia, M.L.**, **Weckwerth, W.** ***et al.*** (2016) The variations in the nuclear proteome reveal new transcription factors and mechanisms involved in UV stress response in *Pinus radiata*. *Journal of Proteomics*, **143**, 390–400.

Passmore, L.A. & **Coller, J.** (2022) Roles of mRNA poly(a) tails in regulation of eukaryotic gene expression. *Nature Reviews. Molecular Cell Biology*, **23**, 93–106.

Pertea, M., **Pertea, G.M.**, **Antonescu, C.M.**, **Chang, T.-C.**, **Mendell, J.T.** & **Salzberg, S.L.** (2015) StringTie enables improved reconstruction of a transcriptome from RNA-seq reads. *Nature Biotechnology*, **33**, 290–295.

Postnikova, O.A. & **Nemchinov, L.G.** (2012) Comparative analysis of microarray data in Arabidopsis transcriptome during compatible interactions with plant viruses. *Virology Journal*, **9**, 101.

Qiu, J., **Xie, J.**, **Chen, Y.**, **Shen, Z.**, **Shi, H.**, **Naqvi, N.I.** ***et al.*** (2022) Warm temperature compromises JA-regulated basal resistance to enhance *Magnaporthe oryzae* infection in rice. *Molecular Plant*, **15**, 723–739.

Ramakrishnan, M., **Rajan, K.S.**, **Mullasseri, S.**, **Palakkal, S.**, **Kalpana, K.**, **Sharma, A.** ***et al.*** (2022) The plant epitranscriptome: revisiting pseudouridine and 2′-O-methyl RNA modifications. *Plant Biotechnology Journal*, **20**, 1241–1256.

Rauf, M., **Arif, M.**, **Fisahn, J.**, **Xue, G.P.**, **Balazadeh, S.** & **Mueller-Roeber, B.** (2013) NAC transcription factor speedy hyponastic growth regulates flooding-induced leaf movement in Arabidopsis. *Plant Cell*, **25**, 4941–4955.

Roundtree, I.A., **Evans, M.E.**, **Pan, T.** & **He, C.** (2017) Dynamic RNA modifications in gene expression regulation. *Cell*, **169**, 1187–1200.

Sadek, J., **Omer, A.**, **Hall, D.**, **Ashour, K.** & **Gallouzi, I.E.** (2019) Alternative polyadenylation and the stress response. *Wiley Interdisciplinary Reviews: RNA*, **10**, e1540.

Salmela, L. & **Rivals, E.** (2014) LoRDEC: accurate and efficient long read error correction. *Bioinformatics*, **30**, 3506–3514.

Sandberg, R., **Neilson, J.R.**, **Sarma, A.**, **Sharp, P.A.** & **Burge, C.B.** (2008) Proliferating cells express mRNAs with shortened 3′ untranslated regions and fewer microRNA target sites. *Science*, **320**, 1643–1647.

Schmitz, R.J., **Hong, L.**, **Michaels, S.** & **Amasino, R.M.** (2005) FRIGIDA-ESSENTIAL 1 interacts genetically with FRIGIDA and FRIGIDA-LIKE 1 to promote the winter-annual habit of *Arabidopsis thaliana*. *Development*, **132**, 5471–5478.

Schwartz, S., **Bernstein, D.A.**, **Mumbach, M.R.**, **Jovanovic, M.**, **Herbst, R.H.**, **León-Ricardo, B.X.** ***et al.*** (2014) Transcriptome-wide mapping reveals widespread dynamic-regulated pseudouridylation of ncRNA and mRNA. *Cell*, **159**, 148–162.

Sett, S., **Prasad, A.** & **Prasad, M.** (2022) Resistance genes on the verge of plant-virus interaction. *Trends in Plant Science*, **27**, 1242–1252.

Shaikhali, J., **de Dios Barajas-Lopéz, J.**, **Ötvös, K.**, **Kremnev, D.**, **Garcia, A.S.**, **Srivastava, V.** ***et al.*** (2012) The CRYPTOCHROME1-dependent response to excess light is mediated through the transcriptional activators ZINC FINGER PROTEIN EXPRESSED IN INFLORESCENCE MERISTEM LIKE1 and ZML2 in Arabidopsis. *Plant Cell*, **24**, 3009–3025.

Shen, Y., **Venu, R.C.**, **Nobuta, K.**, **Wu, X.**, **Notibala, V.**, **Demirci, C.** ***et al.*** (2011) Transcriptome dynamics through alternative polyadenylation in developmental and environmental responses in plants revealed by deep sequencing. *Genome Research*, **21**, 1478–1486.

Shimura, H., **Pantaleo, V.**, **Ishihara, T.**, **Myojo, N.**, **Inaba, J.**, **Sueda, K.** ***et al.*** (2011) A viral satellite RNA induces yellow symptoms on tobacco by targeting a gene involved in chlorophyll biosynthesis using the RNA silencing machinery. *PLoS Pathogens*, **7**, e1002021.

Souza, P.F.N., **Garcia-Ruiz, H.** & **Carvalho, F.E.L.** (2019) What proteomics can reveal about plant-virus interactions? Photosynthesis-related proteins on the spotlight. *Theoretical and Experimental Plant Physiology*, **31**, 227–248.

Su, J., **Yang, L.**, **Zhu, Q.**, **Wu, H.**, **He, Y.**, **Liu, Y.** ***et al.*** (2018) Active photosynthetic inhibition mediated by MPK3/MPK6 is critical to effector-triggered immunity. *PLoS Biology*, **16**, e2004122.

Subtelny, A.O., **Eichhorn, S.W.**, **Chen, G.R.**, **Sive, H.** & **Bartel, D.P.** (2014) Poly(a)-tail profiling reveals an embryonic switch in translational control. *Nature*, **508**, 66–71.

Szklarczyk, D., **Kirsch, R.**, **Koutrouli, M.**, **Nastou, K.**, **Mehryary, F.**, **Hachilif, R.** ***et al.*** (2023) The STRING database in 2023: protein-protein association networks and functional enrichment analyses for any sequenced genome of interest. *Nucleic Acids Research*, **51**, D638–d646.

Tian, B. & **Manley, J.L.** (2017) Alternative polyadenylation of mRNA precursors. *Nature Reviews. Molecular Cell Biology*, **18**, 18–30.

Tian, F., **Yang, D.-C.**, **Meng, Y.-Q.**, **Jin, J.** & **Gao, G.** (2019) PlantRegMap: charting functional regulatory maps in plants. *Nucleic Acids Research*, **48**, D1104–D1113.

Trincado, J.L., **Entizne, J.C.**, **Hysenaj, G.**, **Singh, B.**, **Skalic, M.**, **Elliott, D.J.** ***et al.*** (2018) SUPPA2: fast, accurate, and uncertainty-aware differential splicing analysis across multiple conditions. *Genome Biology*, **19**, 40.

van Loon, L.C. & **Kammen, A.** (1970) Polyacrylamide disc electrophoresis of the soluble leaf proteins from *Nicotiana tabacum* var. "Samsun" and "Samsun NN". II. Changes in protein constitution after infection with tobacco mosaic virus. *Virology*, **40**, 190–211.

Wang, X., **Chang, Z.**, **Zhao, T.**, **Zhong, W.**, **Shi, J.**, **Wang, G.** ***et al.*** (2023) The role of post-transcriptional regulation in SARS-CoV-2 infection and pathogenicity. *Frontiers in Immunology*, **14**, 1256574.

Wang, X., **Lu, Z.**, **Gomez, A.**, **Hon, G.C.**, **Yue, Y.**, **Han, D.** ***et al.*** (2014) N6-methyladenosine-dependent regulation of messenger RNA stability. *Nature*, **505**, 117–120.

Wang, Y., **Zhao, Y.**, **Bollas, A.**, **Wang, Y.** & **Au, K.F.** (2021) Nanopore sequencing technology, bioinformatics and applications. *Nature Biotechnology*, **39**, 1348–1365.

Wiśniewski, J.R., **Zougman, A.**, **Nagaraj, N.** & **Mann, M.** (2009) Universal sample preparation method for proteome analysis. *Nature Methods*, **6**, 359–362.

Workman, R.E., **Tang, A.D.**, **Tang, P.S.**, **Jain, M.**, **Tyson, J.R.**, **Razaghi, R.** ***et al.*** (2019) Nanopore native RNA sequencing of a human poly(a) transcriptome. *Nature Methods*, **16**, 1297–1305.

Wu, L., **Wang, S.**, **Chen, X.**, **Wang, X.**, **Wu, L.**, **Zu, X.** ***et al.*** (2013) Proteomic and phytohormone analysis of the response of maize (*Zea mays* L.) seedlings to sugarcane mosaic virus. *PLoS One*, **8**(7), e70295.

Wu, X. & **Bartel, D.P.** (2017) Widespread influence of 3′-end structures on mammalian mRNA processing and stability. *Cell*, **169**, 905–917.e911.

Wu, X., **Wang, J.**, **Wu, X.**, **Hong, Y.** & **Li, Q.Q.** (2020) Heat shock responsive gene expression modulated by mRNA poly(a) tail length. *Frontiers in Plant Science*, **11**, 1255.

Yang, J., **Worley, E.** & **Udvardi, M.** (2014) A NAP-AAO3 regulatory module promotes chlorophyll degradation via ABA biosynthesis in Arabidopsis leaves. *Plant Cell*, **26**, 4862–4874.

Ye, C., **Zhou, Q.**, **Wu, X.**, **Ji, G.** & **Li, Q.Q.** (2019) Genome-wide alternative polyadenylation dynamics in response to biotic and abiotic stresses in rice. *Ecotoxicology and Environmental Safety*, **183**, 109485.

Yu, F., **Qi, H.**, **Gao, L.**, **Luo, S.**, **Njeri Damaris, R.**, **Ke, Y.** ***et al.*** (2023) Identifying RNA modifications by direct RNA sequencing reveals complexity of Epitranscriptomic dynamics in Rice. *Genomics, Proteomics & Bioinformatics*, **21**, 788–804.

Yu, X., **Wang, Y.**, **Kohnen, M.V.**, **Piao, M.**, **Tu, M.**, **Gao, Y.** ***et al.*** (2019) Large scale profiling of protein isoforms using label-free quantitative proteomics revealed the regulation of nonsense-mediated decay in Moso bamboo (*Phyllostachys edulis*). *Cells*, **8**, 744.

Yuan, S., **Ge, Y.**, **Ling, T.** & **Xu, A.** (2023) Research progress on post-transcriptional regulation of antiviral innate immunity. *Scientia Sinica Vitae*, **53**, 1595–1612.

Zhang, K., **Zhuang, X.**, **Dong, Z.**, **Xu, K.**, **Chen, X.**, **Liu, F.** ***et al.*** (2021) The dynamics of N(6)-methyladenine RNA modification in interactions between rice and plant viruses. *Genome Biology*, **22**, 189.

Zhang, L., **Richards, A.**, **Khalil, A.**, **Wogram, E.**, **Ma, H.**, **Young, R.A.** ***et al.*** (2020) SARS-CoV-2 RNA reverse-transcribed and integrated into the human genome. *BioRxiv* 2020.2012. 2012.422516.

Zhang, T., **Shi, C.**, **Hu, H.**, **Zhang, Z.**, **Wang, Z.**, **Chen, Z.** ***et al.*** (2022) N6-methyladenosine RNA modification promotes viral genomic RNA stability and infection. *Nature Communications*, **13**, 6576.

Zhao, B.S. & **He, C.** (2015) Pseudouridine in a new era of RNA modifications. *Cell Research*, **25**, 153–154.

Zheng, Y., **Yang, D.**, **Rong, J.**, **Chen, L.**, **Zhu, Q.**, **He, T.** ***et al.*** (2022) Allele-aware chromosome-scale assembly of the allopolyploid genome of hexaploid Ma bamboo (*Dendrocalamus latiflorus* Munro). *Journal of Integrative Plant Biology*, **64**, 649–670.